EXPERIMENTAL STUDY ON THE EFFECTS OF A FLOW OBSTACLE ON ANNULAR FLOW IN RELATION WITH *CHF*

R.J. Belt

Delft University of Technology
Department of Applied Physics

Delft, March 2002

Kramers Laboratorium voor Fysische Technologie
Prins Bernhardlaan 6
2628 BW Delft

Professor: prof. dr. ir. T.H.J.J. van der Hagen
Supervisor: prof. dr. R.F. Mudde

Abstract

There is ample evidence in literature that the insertion of flow obstacles in the coolant flow of a boiler postpones the film dryout emergence on the heated surfaces. Specifically, the deposition of droplets forced by the obstacle is believed to increase and is studied in this research.
The two objectives of the present research are (i) to confirm the increase in the film flow rate, this by (ii) building an appropriate flow-loop equipped with suited techniques for film thickness and film velocity measurements.
A cylinder is inserted in the center of a vertical water-air annular tube flow. Variations in liquid film characteristics induced by the obstacle, especially the film thickness and interfacial parameters as disturbance waves velocity and frequency, are measured through (i) a conductance probes technique and (ii) a flow visualization technique. The LDA technique is also tried to be adapted to velocity measurements in the thin film.
The presence of an obstacle in an annular flow leads to an increase in the film thickness, and does not affect the interfacial behavior of the film. An increase in the droplet deposition constant is observed and agrees reasonably well with predictions from the Windecker et al. (1999) correlation. The flow-loop and the measurements techniques are suited for extensive droplet deposition measurements, provided the recommendations are adapted.

Acknowledgement

Hereby, I would like to thank my supervisors Tim van der Hagen and Rob Mudde for their help and guidance during this research.
Also, I would like to thank the technical staff; Jaap Beekman, Jaap Kamminga, Jaap van Raamt and Ab Schinkel, for building the flow-loop.
Finally, I would express my gratitude to dr. Prasser of Rossendorf Forschungszentrum, Germany, for placing the electrode-mesh tomograph to my disposal, for adapting it to my research and for providing me advices.

List of symbols

Roman Symbols

Symbol	Description	S.I. units
C	Droplet concentration	$kg{\cdot}m^{-3}$
C	Parameter in the Katto correlation (1984) (in appendix A)	-
C'	Local droplet concentration at one measurement point	$kg{\cdot}m^{-3}$
C_{obs}	Droplet concentration above the obstacle	$kg{\cdot}m^{-3}$
D	Tube diameter	m
D_H	Hydraulic diameter	m
d_f	Fringe spacing	m
E	Entrainment	-
E_m	Maximal entrainment	-
F	Flow factor defined by Henstock and Hanratty (1976)	-
f	Frequency	Hz
$f(p)$	Parameter in the Biasi correlation (1967) function of the pressure (in appendix A)	-
f_i	Wall friction factor	-
f_o	Fundamental frequency	Hz
f_s	Interfacial friction factor	-
$f_{crossing}$	Doppler frequency shift	Hz
f_{shift}	Frequency shift	Hz
G	Inlet coolant mass flow	$kg{\cdot}s^{-1}$
C	Parameter in the Katto correlation (1984) (in appendix A)	-
$h(p)$	Parameter in the Biasi correlation (1967) function of the pressure (in appendix A)	-
H	Enthalpy of fluid	$J{\cdot}kg^{-1}$
H_L	Enthalpy of saturated liquid	$J{\cdot}kg^{-1}$
H_{LG}	Latent heat of vaporization	$J{\cdot}kg^{-1}$
δH_{SUB}	Enthalpy inlet subcooling	$J{\cdot}kg^{-1}$
k_D	Droplet deposition coefficient	$m{\cdot}s^{-1}$
$k_{D,obs}$	Droplet deposition coefficient with obstacle	$m{\cdot}s^{-1}$
K_i)	Parameter in the Katto correlation (1984) (in appendix A)	-
L	Tube length	m
L_{SP}	Spacing length	m
m	Instantaneous film thickness	m
$\overline{m}$	Mean film thickness	m
m_{obs}	Instantaneous film thickness with obstacle inserted	m

$\overline{m}_{obs}$	Mean film thickness with obstacle inserted	m
m^+	Dimensionless film thickness defined as the ratio of the mean film thickness over the characteristic friction length $\nu_L/\left(\tau_c/\rho_L\right)^{1/2}$	-
$\dot{M}_D$	Deposited water mass flow rate	$kg{\cdot}s^{-1}$
$\dot{M}_{D,obs}$	Deposited water mass flow rate with obstacle	$kg{\cdot}s^{-1}$
$\dot{M}_E$	Entrained mass flow rate	$kg{\cdot}s^{-1}$
$\dot{M}_{E,obs}$	Entrained mass flow rate with obstacle	$kg{\cdot}s^{-1}$
$\dot{M}_L$	Injected water mass flow rate	$kg{\cdot}s^{-1}$
$\dot{M}_{LF}$	Film mass flow rate	$kg{\cdot}s^{-1}$
$\dot{M}_{LFC}$	Critical film mass flow rate	$kg{\cdot}s^{-1}$
N	Records number in the time series	-
p	Pressure	Pa
q''	Surface heat flux	$W{\cdot}m^{-2}$
q''_{CHF}	Critical heat flux	$W{\cdot}m^{-2}$
q''_{obs}	Surface heat flux with obstacle	$W{\cdot}m^{-2}$
$q''_{CHF,obs}$	Critical heat flux with obstacle	$W{\cdot}m^{-2}$
$R'C$	Parameter in the Katto correlation (1984) (in appendix A)	-
R_{CHF}	Relative enhancement in CHF	-
R_D	Droplet deposition rate	$kg{\cdot}m^{-2}{\cdot}s^{-1}$
$R_{D,obs}$	Droplet deposition rate with obstacle	$kg{\cdot}m^{-2}{\cdot}s^{-1}$
R_E	Droplet entrainment rate	$kg{\cdot}m^{-2}{\cdot}s^{-1}$
Re	Reynolds number	-
Re_G	Reynolds number of the core air flow	-
Re_{LF}	Reynolds number of the liquid film	-
Re_{mcr}	Two-phase Reynolds number based on the critical quality	-
s	Ratio of the drop velocity to the gas velocity	-
T	Temperature	K
$T_{surface}$	Wall temperature	K
T_{sat}	Saturation temperature	K
u	Particle velocity	$m{\cdot}s^{-1}$
$\overline{u}$	Mean film velocity	$m{\cdot}s^{-1}$
u_{drop}	Droplet velocity	$m{\cdot}s^{-1}$
u_G	Air velocity	$m{\cdot}s^{-1}$
u_x	particle velocity component perpendicular to the fringes	$m{\cdot}s^{-1}$
ΔV	Increase of volume above the obstacle between two axial locations	m^3
W'	Parameter in the Katto correlation (1984) (in appendix A)	-
x	Thermodynamic quality	-
Δx	Distance between the obstacle and one of the measurement points in mass balance	m
x_{an}	Thermodynamic quality at the onset of the annular flow regime	-
x_{in}	Thermodynamic quality at the tube inlet	-
x_{cr}	Local thermodynamic quality at the dryout	-
x_{cr}^{lim}	Limiting critical quality	-
X_i	Parameter in the Katto correlation (1984) (in appendix A)	-
z	Axial coordinate of the tube	m
Δz	Distance between the obstacle and one of the measurement points	m
z_{SC}	Length of tube under subcooled conditions	m
Z'	Parameter in the Katto correlation (1984) (in appendix A)	-

Greek Symbols

Symbol	Description	S.I. units
β	angle between the direction of particle motion and the normal to the bisector of the laser beams	rad
ϵ	Blockage ratio	-
θ	Angle between laser beams	rad
λ	Wave length	m
μ_L	Liquid dynamic viscosity	Pa·s
ν_G	Air kinematic viscosity	$m^2 \cdot s^{-1}$
ν_L	Liquid kinematic viscosity	$m^2 \cdot s^{-1}$
ρ_G	Air density	$kg \cdot m^{-3}$
ρ_L	Liquid density	$kg \cdot m^{-3}$
σ	Standard deviation (in section 4.6)	-
σ	Surface tension	$kg \cdot m^{-2}$
τ_c	Characteristic shear stress	$kg \cdot m^{-1} \cdot s^{-2}$
τ_i	Interfacial shear stress	$kg \cdot m^{-1} \cdot s^{-2}$
τ_w	Wall shear stress	$kg \cdot m^{-1} \cdot s^{-2}$
ω_o	Pulsation corresponding to the fundamental frequency	$rad \cdot s^{-1}$

Abbreviations

Abbreviation	Description
BWR	Boiling Water Reactor
CDD	Charge Coupled Device camera
CHF	Critical Heat Flux
DNB	Departure from Nucleate Boiling
LDA	Laser Doppler Anemometry

Contents

Chapter 1

Introduction

In industry, the produced heat in exothermic reactors must be eliminated to avoid a too important rise of the reactor's temperature. For that reason, exothermic reactors are often designed with a cooling system, which aims to transfer the produced heat in the reactor to a coolant flow outside the reactor.
For the withdrawal of large amounts of heat, forced boiling and forced evaporation transfer participate essentially to the heat transfer in heat exchangers, referred to as boilers. The latter are much more efficient than simple heating of a single-phase coolant, since the phase transition of liquid to vapor requires more heat than heating of a single phase. This concept is also used in power plant reactors for steam generation.

A crucial safety and economic aspect in boilers is preventing heat fluxes exceeding the Critical Heat Flux (CHF). Beyond the CHF, water contact with the heated surfaces is avoided, with as result, the impossibility of heat withdrawal by evaporation or boiling. Consequently, the heated surfaces rise significantly in temperature and may be damaged.
The interruption of wall-liquid contact exists in different types. This research focuses especially on the film dryout, which is of practical interest. The amount of steam increases progressively in the boiler. A point is reached for which the water-vapor mixture flows in an annular regime, that is, water flows part as a wavy film along the heated surface and part as droplets in the vapor core. In this regime, the crisis arises when the liquid film dries out (see figure 1.1).

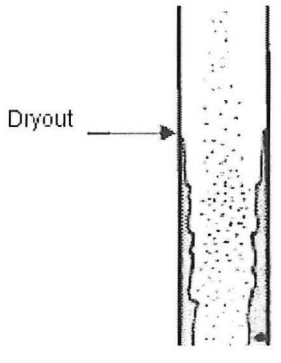

Figure 1.1: Film dryout in annular regime.

Three processes determine the film thickness: evaporation, droplet entrainment and droplet deposition. However, the comprehension of the combined processes is poor. The lack of accurate

modeling leads one to use large safety margins on CHF values predicted from empirical correlations, which results in a reduction of the boiler's performance.

For this reason, one is interested in possibilities to increase the CHF in the annular flow regime. Recent studies have shown an enhancement in CHF when a mechanical flow disturber is inserted. The flow obstacle is believed to increase the deposition of droplets on the film, hence the film mass flow rate, and therefore to delay the dryout emergence.

Enhancement of the CHF (or suppression of its occurrence) will lead to significant economic advantages. For instance, one can refer to (i) increased vapor production in heat exchangers used in chemical industry, (ii) more compact heat transfer equipment and (iii) greater safety margins for aging nuclear reactors, which performance tends to degrade due to fouling of the heat exchangers. One drawback, however, is the higher pressure-drop in the boiler.

This experimental study aims to study the hydrodynamical influence of a flow obstacle on forced droplet deposition in a vertical water-air equilibrium annular flow regime. The film behavior in terms of thickness and velocity is investigated when the obstacle is inserted. Note that no heating source is involved in this research.

In chapter 2, a theoretical approach of the CHF is presented. In chapter 3, the experimental set-up for the measurements of the film characteristics is described. In chapter 4, the results are presented and discussed. In chapter 5, the conclusions and recommendations of this research are given.

Chapter 2

Critical Heat Flux

2.1 Introduction to Critical Heat Flux (CHF)

Forced convective boiling or evaporation of a coolant permit one to evacuate heat efficiently, as the phase transition requires much more heat than simple heating of a single-phase coolant. Water-cooled reactors use in particular this concept by passing a coolant flow on their heated surfaces. Boiling Water Reactors (BWRs) in power plants use forced boiling and evaporation as well for steam production.

Consider the case of vertical heated channels cooled internally by a coolant flow. Forced convective boiling and evaporation alters the flow patterns in the channels, as represented in figure 2.1. The continuous contact of the liquid coolant with the heated surface is not ensured automatically, whereas this is a necessary condition for the heat withdrawal of the wall by boiling and evaporation. A water-cooled reactor unable to eliminate its heat efficiently by boiling or evaporation sees its wall temperature rise significantly and consequently its possible destruction.
Accordingly, a boiling crisis occurs as the surface heat fluxes reach such a level that continuous liquid contact is rendered impossible. The corresponding heat flux is the Critical Heat Flux (CHF). Two types of interruption in the continuous liquid contact with the heated surface exist for heat fluxes exceeding the critical one (see figure 2.1). If the annular flow regime exists (heated channels long enough), the liquid film dries out. In the bubble and slug flow, inadequate removal of the bubbles from the wall makes the presence of dry patches on the wall possible.
The consequence of the boiling crisis is in both cases a drop in heat transfer coefficient, as showed in figure 2.2. The accumulation of heat is expressed in the form of a temperature rise in the wall.

Before continuing, the thermodynamic flow quality x, quantifying the amount of vapor compared to liquid, must be defined. At a distance z of the point where the enthalpy of the vapor-liquid mixture equals that of saturated liquid:

$$x(z) = \frac{H(z) - H_L}{H_{LG}} \tag{2.1}$$

or in terms of heat flux and length:

$$x(z) = \frac{4q''}{DGH_{LG}}(z - z_{SC}) \tag{2.2}$$

where $H(z)$ is the fluid enthalpy at height z, H_L the enthalpy of saturated liquid, H_{LG} the latent

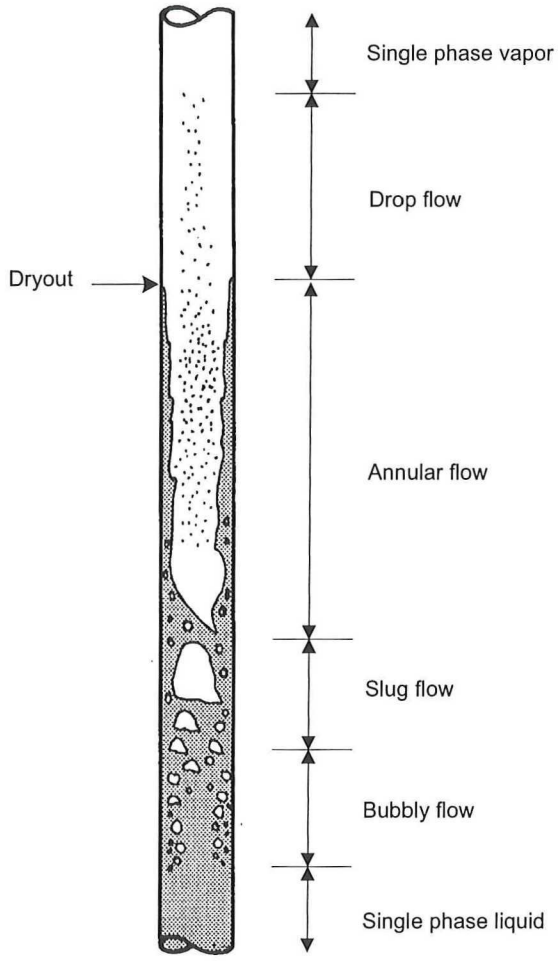

Figure 2.1: Flow regimes in a heated vertical channel.

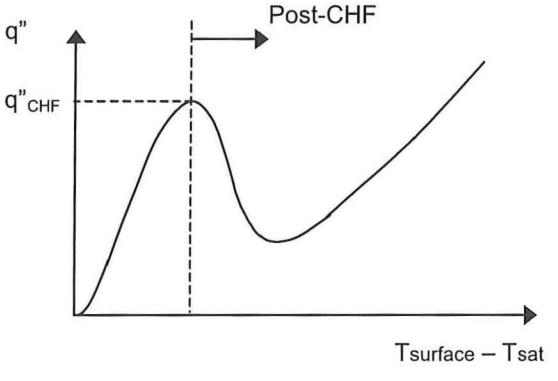

Figure 2.2: Behavior of the heat transfer coefficient with the wall temperature. q'' denotes the transferred heat flux, q''_{CHF} the CHF, $T_{surface}$ the wall temperature and T_{sat} the saturation temperature of the coolant.

heat of vaporization, q'' the surface heat flux, G the coolant mass flux, D the tube diameter and z_{sc} the length of the tube under subcooled conditions.

Interesting is the value of the CHF in both types of crisis. CHF related to the inadequate bubbles removal (Departure of Nucleate Boiling (DNB) type of crisis) is much larger than the one corresponding to dryout. In figure 2.3, the behavior of the CHF with quality is represented. The CHF decreases smoothly with quality, except in a narrow quality range, for which the CHF drops strongly even up to 2 to 3 times.

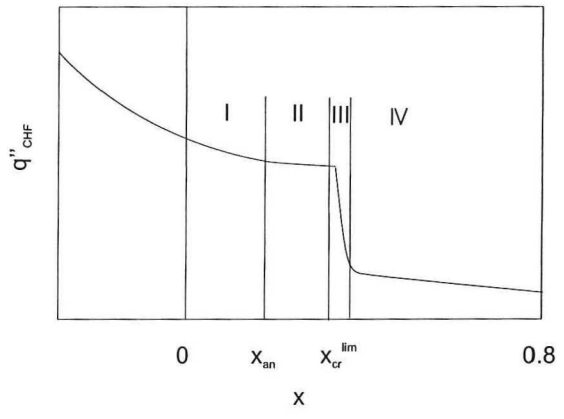

Figure 2.3: Shape of the curve CHF vs.quality for flow boiling of water in circular tubes; pressure $p = 3 - 16MPa$, coolant mass flux $G = 500 - 2500\ kg{\cdot}m^{-2}{\cdot}s^{-1}$; x_{an} the beginning of the annular flow; I the DNB type of crisis at nucleate boiling flow regime; II DNB type of crisis at annular flow regime; III entrainment-controlled dryout type of crisis; IV deposition-controlled dryout type of crisis.

The smallest quality in this critical range, referred as the limiting critical quality, x_{cr}^{lim}, must physically be connected to a change in the crisis mechanism and to the heat transfer regimes (forced convective boiling or evaporation). The drop in CHF occurs in the annular flow regime, the limiting quality being larger than the one for annular regime onset. Operating close to the limiting quality is dangerous. Therefore, it is looked especially for enhancement of the CHF in the annular flow regime. This forms the base of this research.

In the next section, the flow regimes encountered in heated channels with associated heat transfer regimes are described. Consecutively, the CHF mechanisms and prediction methodology are presented briefly in sections 2.3 and 2.4. Finally, the CHF enhancement is discussed in section 2.5.

2.2 Flow regimes

2.2.1 Flow regimes in a uniformly heated channel

The sudden drop in CHF at the limiting critical quality reveals a physical change in the heat transfer regimes (forced boiling or forced evaporation), which are closely related to the encountered flow regimes. Consider the vertical tube heated by a uniform low heat flux and fed at its base with unsaturated liquid, as represented in figure 2.1.
The presence of the heat flux brings either by boiling or evaporation a progressive change in the phase distribution in the tube, related to the production of vapor to the detriment of liquid as

the two-phase flow advances in the tube. Subcooled water enters the tube and is heated up by single-phase convective heat transfer. At a point, the wall temperature reaches that necessary for bubble nucleation and vapor bubbles appear in the continuous liquid phase.
From this point, heat is transferred efficiently by nucleate boiling. Vapor bubbles grow at the nucleation sites and finally detach to form a bubbly flow. When the concentration in bubbles increases, their coalescence forms bubbles of finally a size approximately equal to the tube diameter, which is characteristic of the slug flow. Further nucleate boiling results in an annular flow with a thick film on the wall.
In annular flow, boiling is replaced progressively by evaporation. The film thickness is reduced such that heat transfer through the film is sufficient to prevent liquid in contact with the heated surface being heated to temperatures permitting bubble nucleation. Heat is transferred by forced convection through the liquid film to the liquid-vapor interface, where liquid is evaporated. Furthermore, increasing velocities in the vapor core due to the difference in density causes entrainment of liquid in the form of droplets in the vapor core. Evaporation and entrainment cause a further depletion of the liquid film until the film dries out.
Droplets continue to exist after dryout in the vapor core, forming a drop flow. The droplets are slowly evaporated until single-phase vapor is present. However, heat is transferred through to the vapor to the droplets, consequently, the heat transfer coefficient decreases severely.

Note that the physical processes such as bubble coalescence and droplet formation require time to occur. For rapid changes of the local flow conditions, occurring for instance with high surface heat fluxes, the processes may not be completed and the flow regimes may disappear, be compressed or expanded. For low coolant flow rates, the flow patterns encountered can be completely different, the boiling crisis resulting in an inverted annular flow regime (annular phase distribution but phases inverted).

2.2.2 The annular flow regime

In this research, one is especially interested in the annular flow regime; its most important features for this research are presented below.
In vertical gas-liquid annular flow, part of the liquid flows in the form of a thin and wavy liquid film along the wall and the rest as droplets entrained in the gas core.

The gas velocity is large in annular flow, generally larger than 10 m/s. The interfacial shear causes the appearance of waves on the interface. Two types of waves cover the interface:

- ripple waves, which are small amplitude and short-lived waves,
- disturbance waves, which have an amplitude of about five times the mean film thickness and are axially coherent.

The existence of the waves depends nevertheless on the quantity of water in the film. At low film flow rates, the liquid film is covered by ripple waves. Above a certain liquid film flow rate, disturbance waves surge on the interface. Disturbance waves are via atomization the source of droplet entrainment in the gas core. More specifically, the small waves riding on the top of these disturbance waves break up in droplets.

According to [Schadel et al., 1990] and [Fore and Dukler, 1995a], the critical film flow rate for existence of disturbance waves and of droplets is around 5 g/s and 10 g/s for tube diameters of 2.54 and 4.20 cm, which is larger to the one used in this study (2 cm). The value is approximately

independent of the gas velocity, the variation being smaller than 2%, and decreases in smaller tubes. One can expect a critical film flow rate between 3 and 4 g/s for a tube of 2 cm diameter.

2.3 Mechanisms of CHF

In flow boiling, the CHF mechanisms depend on the distribution of the phases characteristic of the flow regime, which in turn are controlled by mass fluxes, quality and pressure. The flow quality has generally the strongest effect on CHF and determines the boiling crisis mechanism [IAEA, 2001], [Celata et al., 2000], [Collier and Thome, 1994].

In subcooled and low quality regions, inadequate removal of the bubbles from wall causes the boiling crisis. This Departure from Nucleate Boiling (DNB) type of crisis occurs accordingly the following local mechanisms for excessively high surface heat fluxes:

- 'Dryout under a vapor clot' (see figures 2.4 and 2.5). This situation is encountered at high subcooling ($x < 0$). Vapor bubbles grow and collapse at the wall. The boiling crisis is due to the spreading of the dry patch following the evaporation of the thin liquid layer under the stationary bubble. The dry patch may be rewetted after the bubble departure and an alternate but stable situation may be reached. However, at very high heat fluxes, the dry patch can reach such a temperature (Leidenfrost limit) that it cannot be rewetted. Consecutively, the wall surface under the dry patch increases in temperature because of the poor heat transfer.
- 'Bubble crowding and vapor blanketing' (see figure 2.4). This mechanism occurs at moderate subcoolings (approximate quality range from -5% to 5%). A boundary layer of bubbles is formed on the heated surface. This boundary layer grows such that the access of water to the heated surface is rendered impossible. As a consequence, the remaining water is evaporated and a continuous vapor boundary layer is formed on the heated surface, leading to overheating and burnout. This mechanism occurs preferably at the downstream end of the heated channel with this mechanism.
- 'Evaporating of water surrounding a slug flow bubble' (see figure 2.4). In a slug flow regime, the liquid film initially remaining between the slug and the heated surface is evaporated.

In higher quality regions, the flow regime is annular and the boiling crisis arises when the liquid film on the wall dries out.
In the annular flow regime in a heated tube, the liquid film is continuously thinned by evaporation at the interface and by droplet entrainment if entrainment exists. Progressively, the film becomes so small that the disturbance waves are suppressed (due to the laminar layer) and consequently the source of entrainment vanishes. If the net droplet deposition does not balance the evaporation rate, the liquid film breaks down.
Nucleate boiling and the thermocapillary effect can accelerate the dryout mechanism [IAEA, 2001], in particular before the disturbance waves are suppressed. Nucleate boiling can form bubbles, which rupture the film when their size is of the same order of the film thickness. The thermocapillary effect corresponds to the gradient in surface tension existing between the top and the base of the disturbance waves because of the temperature gradient in the film. This gradient tends to move liquid to the top of the waves, which helps to break down the film.

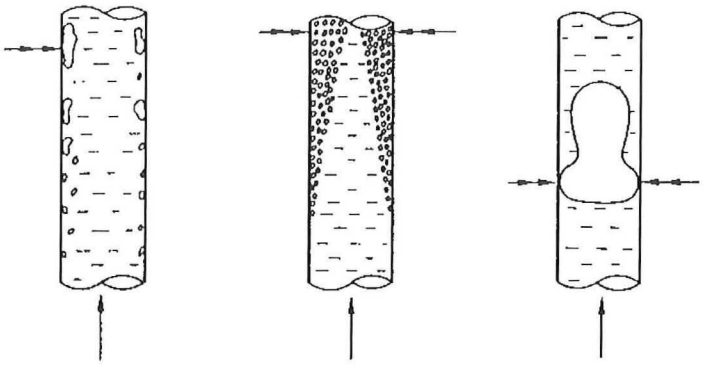

(a) Dryout under a vapor clot.

(b) Bubble crowding and vapor blanketing.

(c) Evaporation of fluid surrounding a slug flow bubble.

Figure 2.4: Mechanisms of the DNB type of crisis. The arrows locate the burnout location.

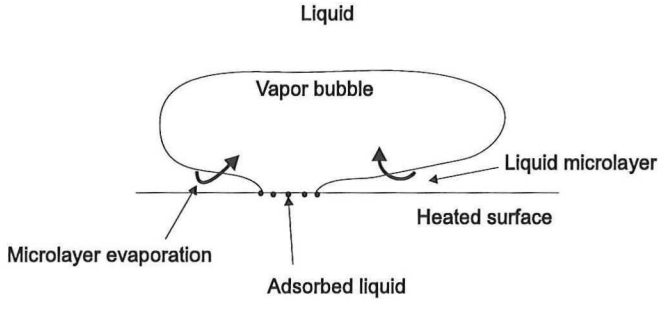

Figure 2.5: Schematization of a dry patch formation under a vapor bubble.

2.4 CHF prediction methodology

First, the orders of magnitude that are relevant for practical cases are 100 to 10000 $kW \cdot m^{-2}$ for the CHF, 0 to 8000 $kg \cdot m^{-2} \cdot s^{-1}$ for the coolant mass flow G and 3 to 200 bars for the pressure p. The geometrical shapes of a water-cooled reactor are various (tubes, bundles). Therefore, CHF prediction with one single method is unfeasible. However, the way of correlating the experimental CHF results does not vary much. Subsequently, a uniformly heated tube flow flowing upwards in a steady state is considered.

Prediction methods of the CHF are mainly empirical relationships. One can think to build empirical correlations based on the inlet conditions. In that case, five main parameters can influence the CHF (denoted by q''_{CHF}): the inlet mass flux G, the inlet subcooling (defined here by the inlet flow quality x_{in}), the heated length L, the tube diameter D and the system pressure p.

$$q''_{CHF} = q''_{CHF}(G, L, D, x_{in}, p) \tag{2.3}$$

On the other hand, one can state that the local CHF is dependent only on the local conditions and not on the upstream history. In that case, we have:

$$q''_{CHF} = q''_{CHF}(G, D, x_{cr}, p) \tag{2.4}$$

where x_{cr} is the local quality at the boiling crisis. Note that a heat balance relates both qualities x_{in} and x_{cr} over the tube. The last approach is the most common one.

The number of empirical correlations is very large, although none of them have been found capable of predicting the CHF over a wide range of flow parameters. For more information about these and their approaches, the reader is referred to [IAEA, 2001] and [Katto, 1994] and to appendix A. Correction methods and some analytical models are furnished as well in [IAEA, 2001].

The CHF look-up table is another prediction approach. This one consists of a CHF database, in which experimental CHF results are collected for tubes with a vertical upward flow of a steam-water mixture. The look-up table approach is built on the 'local-condition' assumption; it provides for discrete values of pressure, mass flux and critical quality the experimental CHF values for 8 mm tubes. An empirical correction factor is introduced for tube diameters different from 8 mm, which is determined from experiments at different tube diameters. The last updated version of the look-up table is found in [Groeneveld et al., 1996] and is far more used nowadays than correlations. Although the diameter effect on CHF is rather complicate, the CHF and the limiting critical quality can be estimated with simple correlations for tube diameters different of 8 mm. The reader is also referred to this look-up table to find the effects of the other cited parameters (p, G, x) on CHF. A global effect of these parameters cannot be described, although it has been done in contradictory ways in literature [Collier and Thome, 1994] and [Corradini, 1997].

2.5 CHF enhancement

In the dryout type of crisis, the liquid film dries out, whereas a large quantity of water exists in the form of droplets. When these droplets can be guided to the wall, the quantity of water in the film is increased and dryout can be postponed.
The idea is to insert a mechanical flow disturber to force the deposition of droplets to the wall. The

enhancement of the droplet deposition rate is believed to be favored by two mechanisms, namely: (i) the droplets blocked by the obstacle are slung to the wall in a straight line following the gas flow and (ii) the droplets are deposited on the wall following the turbulent diffusion mechanism [Binder and Hanratty, 1991], which is enhanced due to the increase in turbulence downstream the obstacle. Finally, heat transfer from wall to the coolant is also improved by the increase in turbulence.

According to literature, obstacles have a positive effect on the CHF caused by the DNB mechanism as well, because of the increase in turbulence, leading to better heat transfer and better bubble detachment.
However, the knowledge of the physical effects of flow obstacles on the CHF is weak. This research attempts to give more information on droplet deposition forced by an obstacle.

CHF enhancement is essential in industrial heat exchangers, as it leads to significant advantages: higher reliability and greater CHF margins on the one hand and higher performance, increased vapor production and more compact equipment on the other hand can be achieved. One drawback of the obstacle is the increase of the pressure drop.

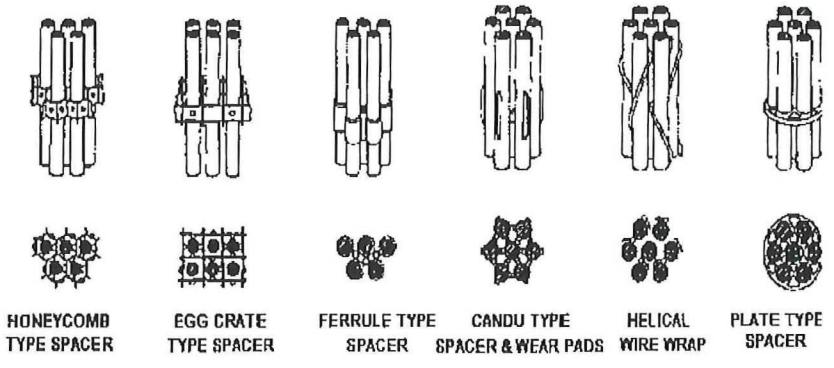

Figure 2.6: Spacers used in rod bundles.

Obstacles in the form of spacers (see figure 2.6) are placed in BWRs in order to maintain an appropriate rod-to-rod clearance. Practically, the spacers influence the flow distribution.

In the DNB as well as in the dryout-type of crisis, CHF enhancement can be stated to be due to the increase in turbulence by the flow obstacle. As the turbulence decreases with distance downstream from the obstacle, the correlation for CHF enhancement considers an exponential decay of the CHF enhancement with distance. For instance, in rod bundles, the relative CHF enhancement, R_{CHF}, due to the use of spacers is expressed by [IAEA, 2001];

$$R_{CHF} = \frac{q''_{CHF,obs}}{q''_{CHF}} - 1 = Ae^{-B\frac{L_{SP}}{D}} \tag{2.5}$$

where $q''_{CHF,obs}$ is the CHF with obstacle inserted, L_{SP} the length between spacers, A and B parameters defined by;

$$A = 1.5\,(0.001G)^{0.2}\,K^{0.5} \qquad B = 0.1 \tag{2.6}$$

and K is the pressure drop coefficient of the spacing device. Recently, [Yano et al.,] have proposed a mechanistic modeling for ring-type spacers.

[Doerffer et al., 1996] and [Pioro et al., 2000] have studied the influence of the obstacles represented in figure 2.7. They found a positive effect of flow obstacles on CHF, but do not report correlations of their results. One study [Guo et al., 2001] proposes a more or less physical approach and makes a distinction between the mechanisms of boiling crisis according the critical quality. In the following part, only the dryout type of crisis is considered.
In the region of annular flow, in which the disturbance waves are suppressed, the mass balance over an incremental distance gives:

$$\frac{d\dot{M}_{LF}}{dz} = (k_D C - R_E - \frac{q''}{H_{LG}})\pi D \tag{2.7}$$

where $\dot{M}_{LF}$ is the water mass flow of the film, k_D the droplet deposition coefficient, C the droplets mass concentration, R_E the droplets entrainment rate and q'' the surface heat flux. The liquid film on the heated surface is very thin; consequently, the droplet entrainment rate and the gradient in the film mass flow can be neglected. The CHF is proportional in this model to the droplet deposition coefficient.
The relative increase in the deposition rates is modeled in [Guo et al., 2001] as a function only of the blockage area, ϵ. Furthermore, the Reynolds number is included in the CHF enhancement correlation, as the droplet deposition rates seem experimentally to increase slower with increasing Reynolds numbers. The effects are all supposed to decay exponentially with distance downstream from the obstacle. As a consequence, the following equation is proposed for the CHF enhancement:

$$R_{CHF} = \frac{q''_{CHF,obs}}{q''_{CHF}} - 1 = c_1 \frac{k_{D,obs} - k_D}{k_D} Re_G^m e^{-c_2 L_{SP}/D} \tag{2.8}$$

where $k_{D,obs}$ is the droplet deposition coefficient with obstacle inserted in the flow, Re_G the Reynolds number of the gas flow and c_1, c_2 and m constants determined experimentally. Based on experimental data for Freon and on other studies, [Guo et al., 2001] propose for the relative increase in the droplet deposition rates:

$$\frac{k_{D,obs} - k_D}{k_D} = 1.4416\epsilon^{0.65} \tag{2.9}$$

and for the constants:

$$m = -2/3 \qquad c_1 = 1.9 \cdot 10^5/1.4416 \qquad c_2 = 1 \cdot 10^{-6} Re_{mcr}^{0.8} \tag{2.10}$$

where Re_{mcr} is the two-phase Reynolds number based on the critical quality and equals $GD/\mu_L[(1-x_{cr}) + x_{cr}\rho_G/\rho_L]$, μ_L being the liquid viscosity, ρ_G and ρ_L respectively the gas and liquid density.

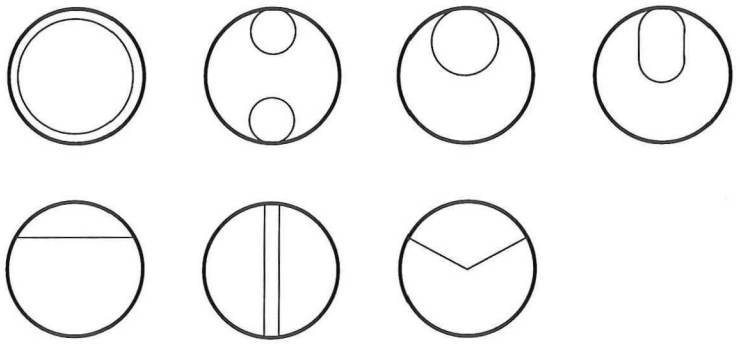

Figure 2.7: Obstacles used in literature studies on CHF enhancement.

Chapter 3

Experimental set-up

3.1 Flow-loop

This research attempts to measure the effects of an obstacle on:

- the film thickness
- the velocity profile in the film
- the shape of the film

The flow loop, represented in figure 3.1, is built for this purpose. Parameters in the flow-loop and in the operation conditions are chosen to obtain a vertical upward co-current annular air-water flow, in which the water film is very thin ($m \ll 1$mm) and the air stream laden with droplets.
The main component is the 5 m long Perspex vertical tube of 20 mm internal diameter. Pressurized air is introduced at the bottom of the tube and passes through a calming section of 25 tube diameters length. Then water is injected with a pump into the tube using a special entry device shown in figures 3.3.c and 3.3.d. Water enters the tube axially through an annulus. So, water and air are contacted in a distribution already annular and the equilibrium annular flow is expected to be reached over a short distance. According to literature [Fore and Dukler, 1995a] [Schadel et al., 1990], a developing length equivalent to 150 column diameters before the test section is sufficient with such a device. The volume flows of air and water are measured with appropriate rotameters. For air, a rotameter able to measure air flows between 8.3 and 33.3 L/s is used. A bank of two rotameters is used to measure the volume flow of water entering the tube, one for small flows (from 3 to 30 g/s) and one for high flows (from 15 to 70 g/s).
The test section consists of the part of the column containing the flow obstacle and the measurement probes. Its length is equivalent to 75 column diameters, which is felt to be sufficient to return to the equilibrium annular flow. The flow obstacles effects on CHF disappear after a length equivalent to 50 column diameters according to [Doerffer et al., 1996] and [Pioro et al., 2000]. The test section is build of segments, which are fitted to each other. The advantage is a completely modulable test section, where the measurements stations and the flow obstacle, consisting each of segments, can be shifted along the test section. The segments are 10 cm long; one is illustrated in figure 3.2.
The liquid film is separated from the droplets laden air flow downstream the test section to measure the film and entrained mass flows. The film withdrawal device, illustrated in figures 3.3.c and 3.3.d, is identical to the film generator but placed upside down. Both outputs of the tube, after a flow

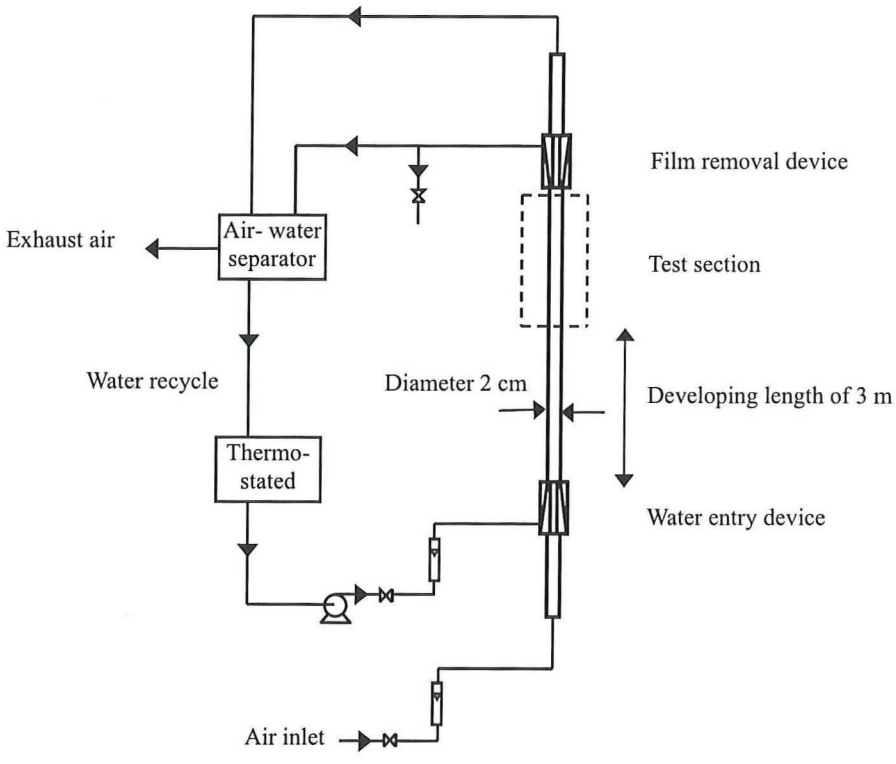

Figure 3.1: Flow-loop.

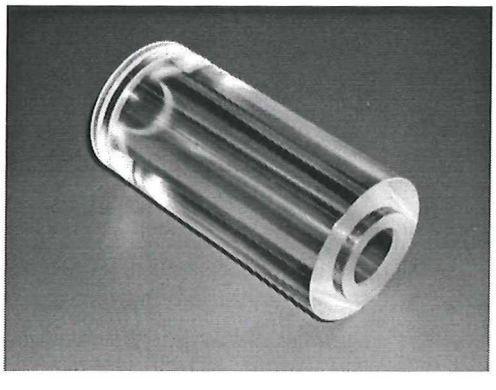

Figure 3.2: Segment.

weighting possibility, fill a separation reservoir open to atmosphere. With this reservoir, air is exhausted from the flow-loop whereas water is recycled to a thermostatic reservoir. The latter intends to keep water in the flow-loop at a constant temperature of approximately 20^oC, necessary for film thickness measurements by the conductance probes. The film thickness is derived by calibration of the probe, which is performed with loop-water at 20^oC. A temperature deviation of 1^oC during the measurements causes typically a deviation of about 2.5 % in the water conductivity [Coney, 1973]. The same deviation is obtained in the derived film thickness, as the latter is proportional to the water conductivity.
The flow obstruction used is a cylinder of 1 cm diameter and 1 cm height and is held on the column axis by three metal spokes of 1 mm diameter (see figures 3.3.a and 3.3.b).

In this research, the air velocity is between 30 and 100 m/s (measurements are performed at 32, 40, 50, 61, 69, 77 m/s), as high interfacial shear is required for droplet entrainment. To reach such velocities, the choice of the internal diameter of the column must be appropriate (20 mm). In this research, water mass flow rates of 4.7 to 60 g/s are used. The water flow rates must be around and larger to the critical flow rate, which can be estimated equal to a value between 3 and 4 g/s according to the results of [Schadel et al., 1990] and [Fore and Dukler, 1995a].

Film characteristics are measured by three different techniques. Laser-Doppler Anemometry aims to measure locally the velocity of the liquid film. Conductance measurements intend to measure the instantaneous film thickness, leading to (i) the mean film thickness, the maximum film height and the thickness of the film substrate and (ii) the disturbance waves velocity and the power spectrum of the film thickness modulations. Flow visualization by a fast video camera reveals characteristics of the film interface, as velocity and passage frequency of the disturbance waves, and is used to validate the measurements by the other techniques. The measurement techniques are discussed in next sections.

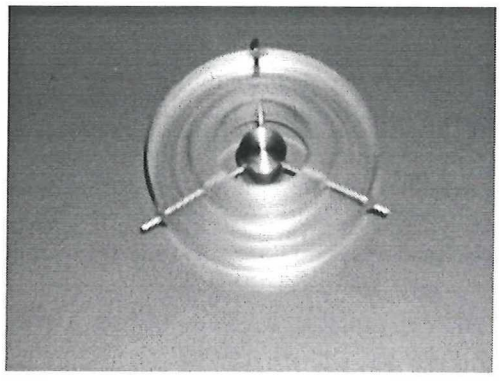

(a) Obstacle.

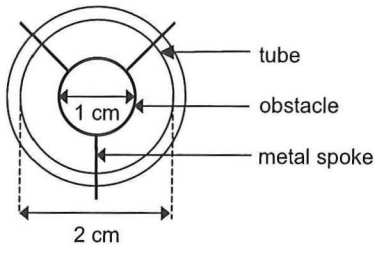

(b) Schematic representation of the segment containing the obstacle.

(c) Device for film withdrawal from the tube and also for water entry (but device upside down in that case).

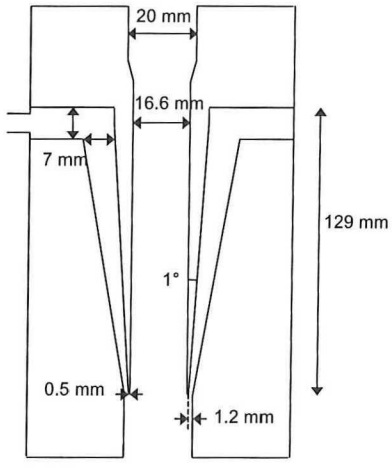

(d) Schematic representation of the film removal device.

Figure 3.3: Devices used in the flow-loop.

3.2 Conductance probes

Objective of the present experiment involving conductance is to determine in a vertical annular flow the film thickness and the disturbance waves velocity.

Conductance experiments are based on the annular phase distribution and the electrical conduction properties of water and air. In an air-water annular flow regime, water is distributed partly as a wavy film along the wall and the rest as droplets entrained by the flow of air in the core. As the air core is almost insulating, the conductance of the flow depends only on the electrical conduction in the liquid film.
For two electrodes mounted flush to the wall, the conductance between the electrodes depends on the quantity of water in between. The conductance behaves as (i) a function of the water conductivity acting as proportionality constant in the conductance magnitude, (ii) a decreasing function of distance between the electrodes and (iii) an increasing function of the area of the liquid film across which the current density flows. This area is proportional to the film thickness.
Consequently, for a potential difference applied between the electrodes flush to the wall, the current measures the film thickness between the electrodes. From the current, an almost instantaneous film thickness can be obtained, but averaged over the area between the electrodes.

The disturbance waves traveling on the interface are axially coherent and of large amplitude, hence easily identifiable. One can obtain their axial velocity component by cross-correlating the instantaneous film thickness obtained by two distinct probes, of which the separation distance is known.

The thickness profile in time reveals also additional information about the shape of the film. More particularly, a power spectrum informing about the frequencies in thickness profile can be drawn.

In literature, the film thickness is usually measured with conductance probes; however, it must be noted that other successful methods can be applied for film thickness measurements. For instance, the total internal reflection of light method [Shedd and Newell, 1998] appears to be well adapted for thickness measurements of thin films. Laser-induced fluorescence [Kockx, 1999] can be used as well, albeit for relatively thicker films.

3.2.1 Type of electrodes

The conductance probe used in this study consists of two parallel ring electrodes mounted flush to the wall. The rings extend in this configuration around the column circumference. This type of probe (see figure 3.4) is preferred to other utilizable devices, such as thin wires protruding the film and electrode islands flush to the wall.
First, flush mounted probes are preferred since they do not introduce disturbances into the film contrary to wires probes traversing the film. However, flush probes are characterized in contrast to wire probes by a saturation of their response for film heights larger than the distance between the electrodes [Coney, 1973]. The electrical field cannot expand to the film edge in too thick liquid films (see figure 3.5). Nevertheless, for very thin films in the order of 100 μm, as expected in this research, and for electrodes sufficiently spaced apart, the response is well approximated by a linear relationship increasing with thickness. Furthermore, the conductance measurements stay more or less localized, as the distance between the electrodes can be in the order of millimeters because of the very thin film.
Ring electrodes are more suitable than electrode islands in this research, as the probe with ring electrodes permits a higher sensitivity. The current between the electrodes increases as the area

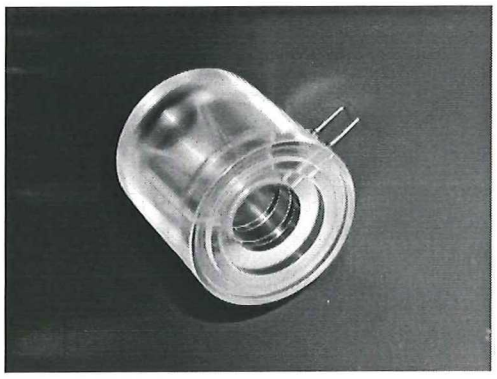

(a) Segment serving as conductance probe.

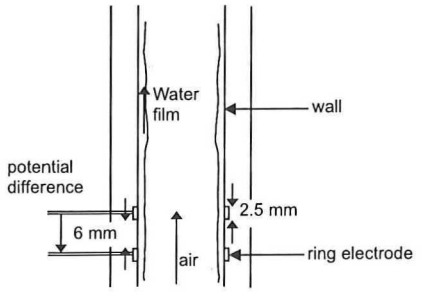

(b) Schematic representation of the conductance probe.

Figure 3.4: Conductance probe.

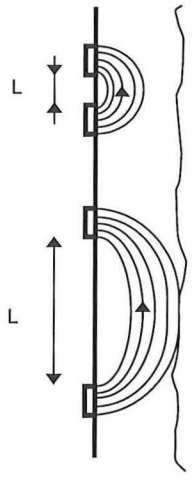

Figure 3.5: Insufficient separation distance leading to saturation of the response and sufficient separation distance, respectively.

left for the passage of current increases; this one is the largest for ring electrodes. The fluctuations are enlarged and small changes in the film thickness can be evaluated, which may be of importance to detect an increase in the film thickness by forced droplet deposition. The principal advantage of electrode islands is the observation of eventual asymmetrical film behavior in the tube, which is not feasible with ring electrodes as this type of probe averages over the tube circumference. However, according to [Asali et al., 1985], the film should behave symmetrically at the large gas velocities used in this research ($v_{air} \geq 25$ m/s). In addition, we are interested in the circumferentially averaged film thickness and the axial velocity component of the disturbance waves, since the insertion of flow obstacles affects the axial location of the CHF.

Another important issue in the design of the conductance probes is the distance separating the electrodes compared to the length of the disturbance wave. For accurate and local measurements of film heights, the distance between electrodes must be significantly smaller than the length of the disturbance wave. Else, the height of the disturbance wave is not measured correctly because of averaging of the height of the disturbance wave with the height of the substrate film (see figure 3.6). Moreover, it is questionable whether the electrical field reaches the top of the disturbance waves when the waves are much smaller than the distance between the electrodes (see figure 3.6.b). The

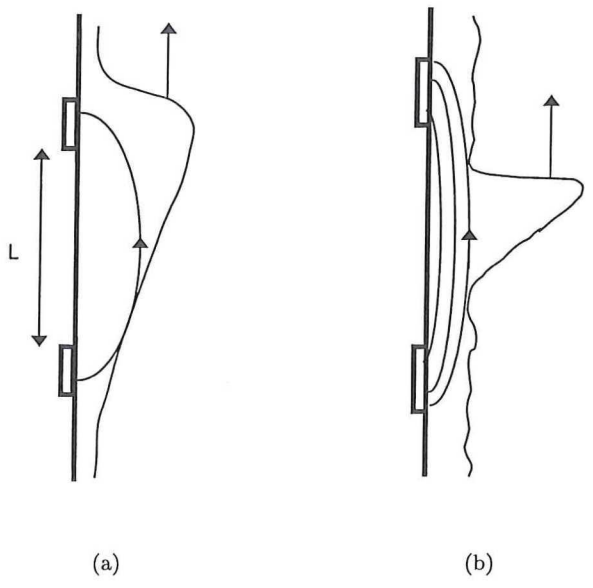

Figure 3.6: (a) Separation distance between the electrodes compared to the length of the waves. (b) The height of the disturbance wave is averaged with the height of the substrate film and the electrical field may not reach the top of the waves.

conductance probe is constructed with a separation of 6 mm between the electrodes. Preliminary results show that this distance is smaller than the length of the disturbance wave. Furthermore, this separation distance avoids a possible saturation of the response, as the distance between electrodes is larger to the maximum expected film height of 1 mm according to literature.

3.2.2 Type of voltage

Chemical and ionic off-equilibrium must be prevented in order to obtain steady and reproducible results. Consequently, the voltage signal supplied to the conductance probe must alternate and be

of sufficiently high frequency, as this avoids sources of ionic gradients or redox reactions. The latter must be prevented, since they cause apparition of small bubbles and dissolution of the electrode's material. Furthermore, the film thickness is derived during the period of the voltage signal. The time profile of the film thickness is higher in time-resolution with a high frequency sampling signal. In literature, signals of frequency above 10 kHz are used. With the equipment used in this research, a frequency of maximum 15 kHz can be reached, and a frequency of 14 kHz is used.
Studies in literature usually apply a sinusoidal voltage [Coney, 1973] [Asali et al., 1985]. In that case, the instantaneous amplitude carrying the information about the conductance is derived by demodulating the signal. However, this demodulation requires a driving frequency of the supply voltage significantly higher than the desired measuring rate, which is already in the order of several kilohertz. However, this is unnecessary, since the electrodes-electrolyte system behaves globally as a RC circuit in series. Consequently, when a rectangular signal is applied to the electrodes, the response can be described as having a transient behavior caused by the capacitance and followed by a constant one (see figure 3.7). The constant signal is a measure of the conductance of the film. The electrodes-electrolyte system is electrically equivalent to a RC circuit in series. The ion migration in the liquid bulk is equivalent to a resistance, which is in series with a capacitance caused by the double layer (charged 'layers' to allow charge transfer from electrode to electrolyte), the electrodes and the cables.
The time of the equivalent RC circuit, $\tau = RC$, is measured with a RCL-meter. This characteristic time is plotted as a function of the film thickness in figure 3.8 for an excitation signal of 10 kHz. The value of τ is smaller than $7{\cdot}10^{-7}$ s; consequently, τ is significantly smaller than the duration of one squared block (1/36 ms). Note that the capacitance and the resistance are measured in a set-up similar to the calibration one (see the section 4.3 below); a plug is inserted in the segment containing the conductance probe, leaving a gap filled with water of known distance. Note also that the resistance of the film decreases as expected with film thickness (from 41.5 kΩ for 60 μm to 6 kΩ for 495 μm) and that the capacitance increases with film thickness (from 6.5 pF for 60 μm to 136 pF for 495 μm).
The procedure of voltage supply is controlled by software. Initially, software is used by [Prasser et al., 1998] in their study on an electrode-mesh tomograph. The control program has been modified in order to make it adequate for the present research.

3.2.3 Insulation electrode

Two measurement stations are used at the same time to determine both the film thickness at two locations and the axial velocity component of the disturbance waves. However, it must be prevented that current transmitted from one probe can be sensed by the receiver of the other probe, even though the distance between the probes is much larger than the one between the electrodes. These parasitic currents corrupt the results. To avoid any interference between the probes, a ring electrode, which is continuously connected to earth, is placed between the two conductance probes. The impedance of the insulation electrode is much smaller than the impedance of the fluid and so hinders the passage of parasitic currents from one probe to the other. Else, a parasitic current of about 6% would be sensed by the 'wrong' receiver, as this one is located 10 cm from the transmitter supposed to excite the 'right' receiver separated of a distance of 0.6 cm. This issue is verified in preliminary measurements.
Note also that the transmitters and receivers are designed with an impedance significantly lower than the impedance of the fluid. This guarantees a zero potential continuously at the receiver electrodes. Consequently, any parasitic potential difference giving rise to parasitic electrical currents is prevented.

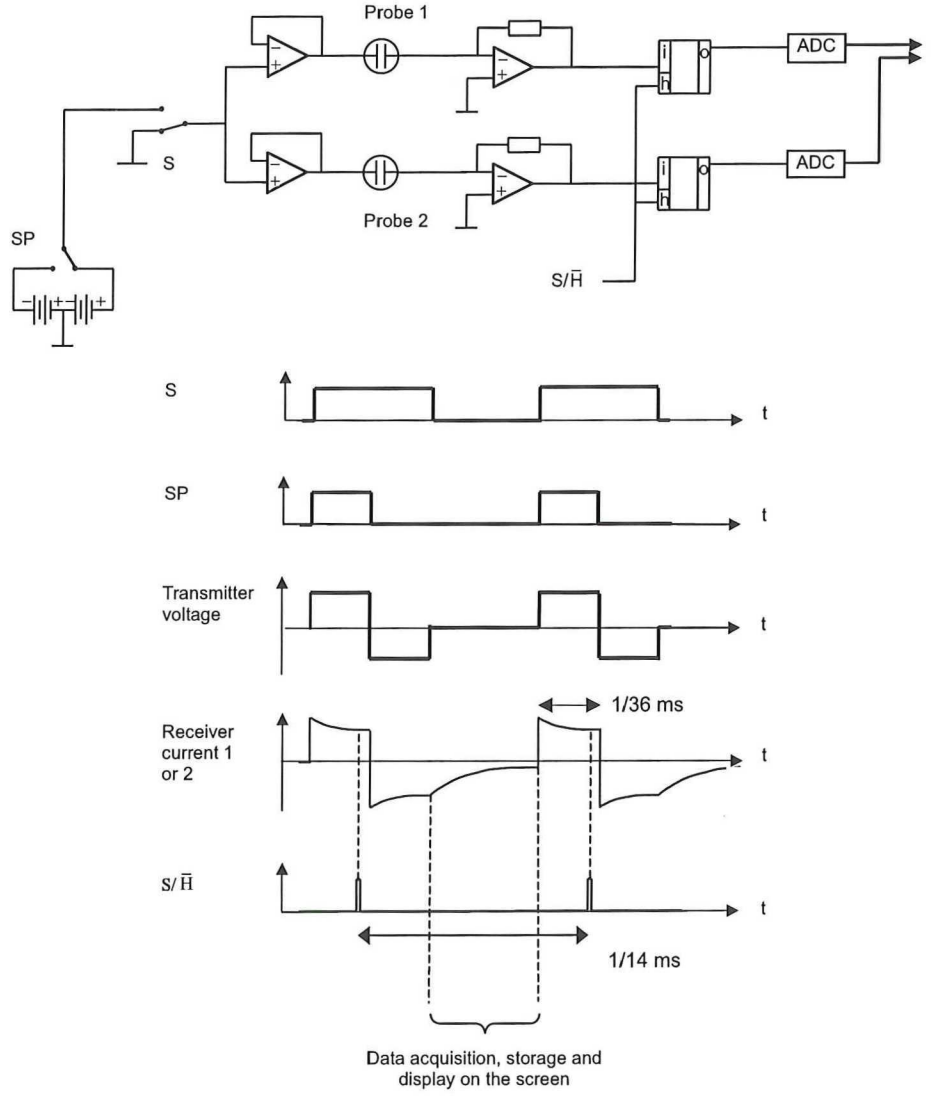

Figure 3.7: Schematization of the steps in the measurement procedure.

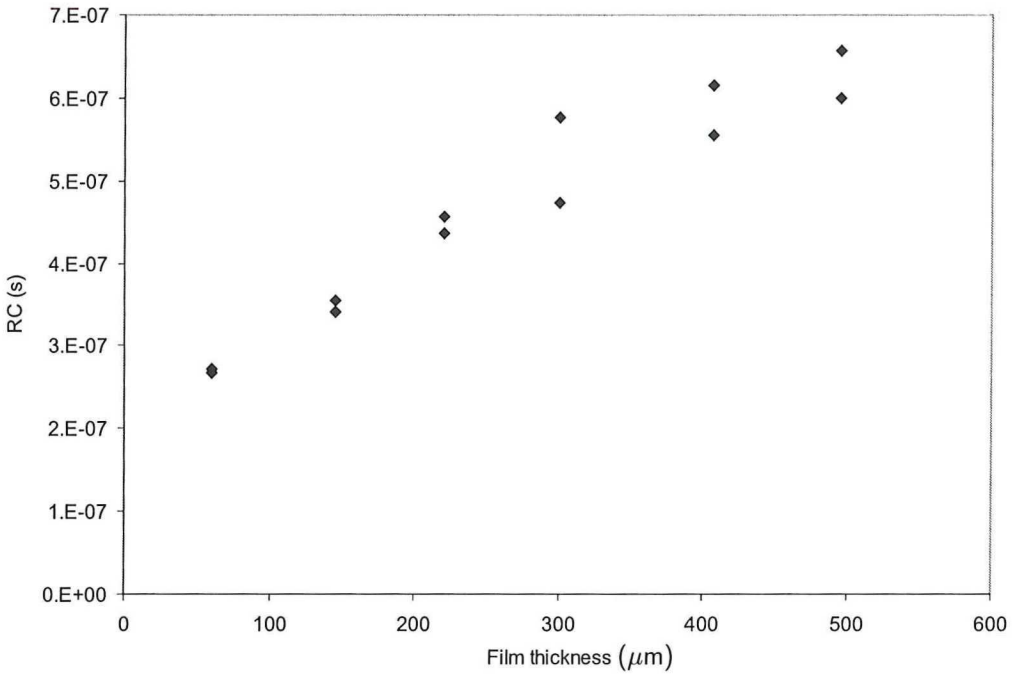

Figure 3.8: Characteristic RC time as a function of the film thickness.

3.2.4 Construction of the conductance probe

Software for data acquisition, data storage and voltage supply as well as hardware is provided by dr. Prasser of the Forschungszentrum Rossendorf in Germany.
The procedure is illustrated in figure 3.7. The rectangular voltage is made of two direct voltages, which are alternately supplied to the probes. Both conductance probes are supplied by the same excitation signal of maximum frequency 15 kHz. Each receiver is followed by an amplifier-reverser circuit, which transforms the current from the probe into a voltage proportional to the probe's conductance. Next, useful values of this signal are sampled; that is, values when the transient behavior has settled down. In this way, the sampled signals reflect only the direct component associated to the conductance between the electrodes. The sampling procedure is performed with the help of individual sample/hold circuits. Finally, the analogue signals are converted in digital signals, which are recorded by a data acquisition computer.

The conductance probes are schematized in figure 3.4 and in figure 3.9. The complete test section consists of segments of 10 cm long. The conductance probes consist of segments as well; the advantage is that the probes can be placed at various positions along the column. The segment containing the conductance probe is 5 cm long and is associated with another dummy one of 5 cm long as well. Consequently, both segments have the same length as the main segments enabling to perform each 5 cm thickness measurements. The wave velocity is obtained by cross-correlating thickness measurements obtained by two conductance probes separated by a distance of 10 cm. To avoid interference between the two probes, one segment of 5 cm long containing the insulation electrode separates the segments containing the conductance probes.
Height in axial direction of one electrode is 2.5 mm; the separation distance between the electrode rings is 6 mm. Each electrode is made of a ring of stainless steel of internal diameter exactly 20 mm and of external diameter 25 mm. Rings are inserted into grooves made into the segments by cutting it (a small space can exist in between). Note that the ring electrode configuration has the

disadvantage of being difficult to construct.

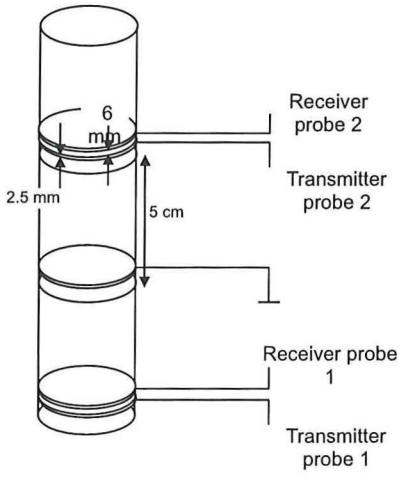

Figure 3.9: Schema of the conductance probes.

3.2.5 Calibration

A theoretical approach exists to determine from the current measurement the corresponding film thickness; however, the theory is only valid for voltages supplied to the electrodes at very high frequencies (in the order of 500 kHz) according to studies in literature [Coney, 1973] [Brown et al., 1978] [Asali et al., 1985]. However, working with such high frequency is unnecessary and the film thickness is obtained by calibration measurements instead.

The calibration is performed with static liquid in the conductance probe. Different PVC plugs of diameter smaller than 2 cm are inserted in the conductance probes. For each plug, the gap between the plug and the probe wall is filled with water and a static calibration is performed. 7 plugs are used in the calibration leaving a gap between 60 and 600 μm, which is in the same order of the film heights encountered in the experiments. Care is taken to have the plugs correctly centered in the conductance probe. For this purpose, the plugs are machined such that they can be joined to the conductance probe like the other segments. As small differences can exist between the two conductance probes, both are calibrated separately.
The calibration curves are shown and discussed in section 4.3.

3.3 Liquid film visualization with a fast video-camera

The visualization to the naked eye of the vertical annular pipe flow shows a milky appearance of the liquid film corresponding to the waves structure on the gas-liquid interface. Frequencies of the waves are in general superior to the maximum time-resolution of the naked eye (which is in the order of 20 Hz); as a result, a milky or averaged film structure is observed instead of distinguishable waves.
From this originates the idea to use a high-speed video camera to photograph the liquid film, which provides consecutive images of the liquid film separated by a small time-step. As the time-step is small compared to the wave period, characteristics of the liquid film, more particularly of the waves, can be obtained.

3.3.1 Observation

The main information one can obtain from a video film is the roughness of the interfacial structure of the liquid film.
The photographed images are explained by the interface behavior. Ripple waves and disturbance waves differ in amplitude; the ripple waves being small and the disturbance being large compared to the mean film thickness. In addition, the disturbance waves are turbulent with large variations in the waves interfacial surface. The surface of the disturbance waves is rough compared to the ripple waves one.
Rough surfaces scatter much more light than smooth surfaces. As light reflection by the interface is visualized on the video film, the disturbance waves, corresponding to the zones of large light intensity variations, are located in the images. Knowing the time-step between successive images, one can derive:

- the velocity of the disturbance waves.
- the passage frequency of disturbance waves at a certain axial location.

Furthermore, the length of the disturbance waves can be obtained.
However, the liquid film thickness cannot be determined with this technique because of the rounded surface. Visualization of the film thickness would be in the direction perpendicular to the camera direction. Because of the rounded surface of the tube, one has to traverse the liquid film, which hinders an accurate determination of the film thickness (see figure 3.10).

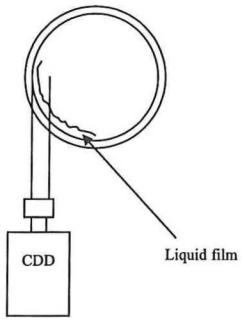

Figure 3.10: Representation of the set-up showing the impossibility to measure the film thickness.

3.3.2 Use of strobe light

The video camera used in experiments photographs the structure of the liquid film each 1/400 s; the shutter is open during 1/200 s per image. However, the time step is not short enough to capture the film structure. For instance, if one considers a disturbance wave moving at 4 m/s, it has traveled a distance of 5 mm in one photographed image. This means that a punctual element of the disturbance wave will have on the photographed image an axial length of 5 mm. The characteristic lengths of the disturbance waves should be at least a magnitude higher than these streaks.
This blurring effect can be avoided by 'freezing' the liquid film by strobe lights when photographing. Flashes of the strobe light last only 30 μm, sensibly less than the photography rate equal to 2.5 ms/frame. So, the photographed images do visualize the liquid film during the flash period of 30 μs instead of the photographing period of 1/400 s. A punctual element of a disturbance wave moving at 4 m/s has traveled in the photographed image a distance of 0.12 mm instead of 5 mm, which shows the increase in accuracy.
The flashes are triggered by the video camera in order to have one flash per photograph. The position of the strobe light must be correct, as light reflected by the column wall should not fall directly on the video camera lens. Else, a bright white patch due to wall reflection will be obtained. The light source should be illuminating the recording section either sideways or from above/below, but should not be placed in the same direction as the video camera. In this research, the strobe light illuminates the test section from above.

3.3.3 Data analysis

One is referred to figure 3.11 to understand the data analysis procedure. Figure 3.11 shows two images photographed consecutively. Because of the difference in roughness between the two types of waves, it is believed that the strong undulations in light intensity on the images are characteristic of disturbance waves, whereas the smooth appearance on the images corresponds to the liquid film covered by ripple waves.

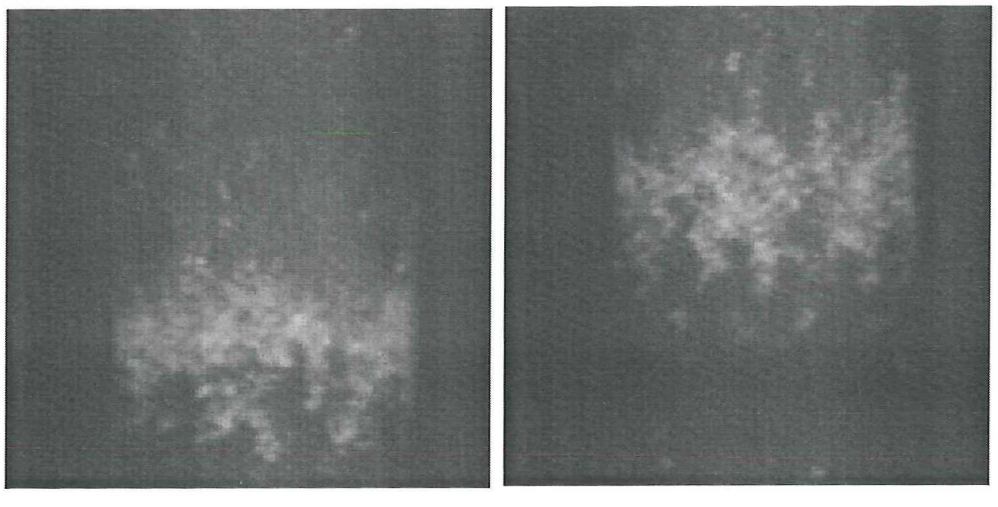

(a) Image i. (b) Image i+1.

Figure 3.11: Two consecutive images separated by a time step of 1/400 s.

According to literature [Wolf et al., 1996], [Azzopardi, 1986], disturbance waves are said to be coherent over long axial distances. However, one can state that principally mean characteristics of the disturbance wave as axial length and mean velocity are meant. The interfacial structure of the disturbance waves is assumed to vary in time/location because of turbulence.
The structure in the surface of the disturbance changes, but cannot have changed completely between two consecutive photographed images. A cross-correlation technique is used, which attempts to identify the same waves on the surface of the disturbance waves and consequently to measure the displacement of the disturbance wave. The two images are superposed with a shift in order to match the images at best and a cross-correlation factor is estimated. A feature in cross-correlation is that the correlation estimates are biased because of the finite record length [Raffel et al., 1998]. With increasing shifts, less data are correlated with each other because of the smaller overlapping. Unless the correlation values are weighted accordingly, the displacement estimate will be biased to a lower value (see figure 3.12). The bias error is corrected in all cross-correlation techniques used.

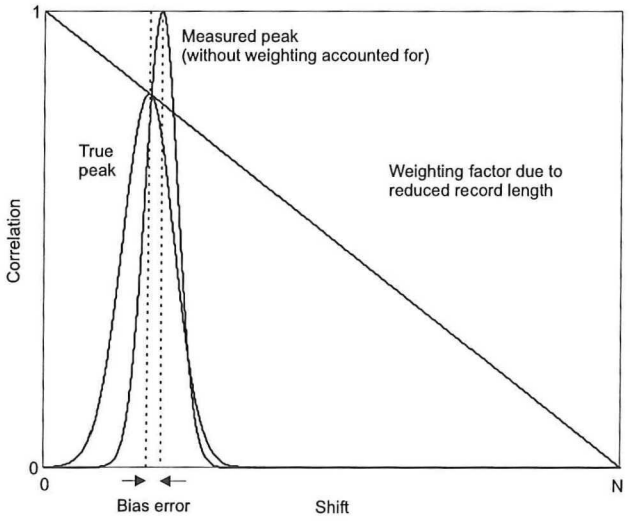

Figure 3.12: Bias in the cross-correlation technique.

3.3.4 Design

The set-up is schematized in figure 3.13.

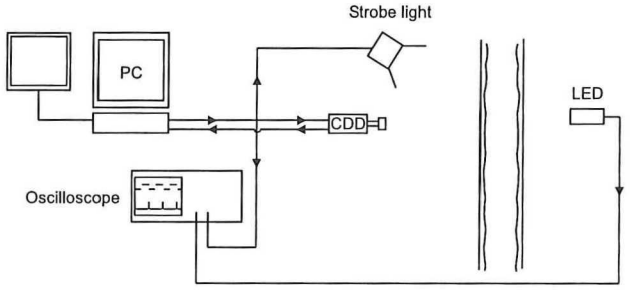

Figure 3.13: Experimental set-up.

A Dalsa Inc. video camera is used; the maximum film rate is 750 frames per second. Data is

acquired with an IRS camera system software installed on a SunOs Unix terminal. Resolution of the video camera is 128 pixels in width and 126 in height.
Flashes illuminating the liquid film are furnished by a GR 1540 Strobolume stroboscope. It is desired to have one flash each photography-shooting period; therefore, the stroboscope is triggered by the video camera software. The stroboscope can deliver flashes at a frequency of maximal 400 Hz. So, the filming rate of the video camera cannot exceed 400 Hz, else flashes will be missed in certain images, leading in that case to completely dark images. For verification, a LED is used to visualize on an oscilloscope the strobe light frequency and the length of the flash. The installation is schematized in figure 3.13.
Data is analyzed by Scilimage 1.4.1 software, supplemented by self-made c++ subroutines.

3.4 Laser-Doppler Anemometry

Laser-Doppler anemometry (LDA) is a non-intrusive optical technique permitting one to measure velocities in a flow. In this research, it is tried to adapt the LDA technique to velocity measurements in the very thin liquid film, which thickness is in the order of the measurement volume. Only preliminary LDA experiments were performed on a flow-loop, in which the flow was transitional. Nevertheless, it is indicated that physical trends of the liquid film are measured, albeit unclear for the moment what velocity is actually obtained.
The LDA theory is explained first; then the results of LDA experiments in a preliminary flow-loop are described, accompanied by interpretations and recommendations. It is chosen to report the LDA technique by incorporating the preliminary results, as this may show how this technique has to be developed further for velocity measurements in a thin liquid film.

3.4.1 Fringe model

The fringe model is a simple approach to describe LDA, although this model does not fully reflect reality. Consider two intersecting and quasi-parallel light beams (see figure 3.14), which have a sufficiently defined frequency, as it is the case in laser light, and a phase relationship. The coherence condition is satisfied and the light beams can interfere. A fringe system consisting of bright and dark bands appears in the cross-region of the beams. The distance between the intensity maxima, called fringe spacing d_f, equals:

$$d_f = \frac{\lambda}{2 \sin \frac{\theta}{2}} \tag{3.1}$$

where λ is the wavelength of the laser light and θ the angle between two laser beams.

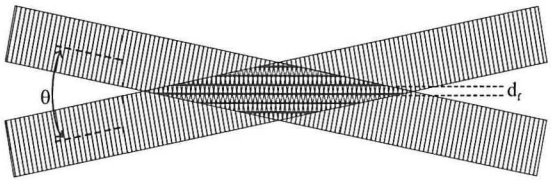

Figure 3.14: Interference pattern of two intersecting laser beams.

Small particles crossing the fringes will scatter light with an intensity modulation depending on the passage of the particles in the fringe pattern. The frequency in intensity modulations of scattered light, $f_{crossing}$, is proportional to the particle velocity component in the direction normal to the fringe planes, u_x:

$$f_{crossing} = \frac{u_x}{d_f} = \frac{2u}{\lambda} \sin \frac{\theta}{2} \cos \beta \tag{3.2}$$

where u is the particle velocity and β is the angle between the direction of the particle and the normal to the fringe planes.
The frequency $f_{crossing}$ is equal to the Doppler frequency shift. The fringe model informs about a velocity component by determining the Doppler shift, but fails in the sense that fringes do not exist in the cross-region. Applications exist in which the fringe model fails; therefore, the simple-in-handling model must be used with care. The reader is referred to [Drain, 1980] for a detailed description of LDA.

3.4.2 Frequency shift

The Doppler shift informs about the absolute magnitude of the velocity component, but does not give the velocity direction. Commonly frequency shifting is used to solve this. The idea is to apply to one of the incident beams a constant frequency shift f_{shift}. This frequency shift produces a frequency offset; one measures the original Doppler shift added by the frequency shift:

$$\Delta f = f_{shift} + \frac{2u}{\lambda} \sin\frac{\theta}{2} \cos\beta \tag{3.3}$$

The position of the value of Δf compared to f_{shift} informs about the sign of the velocity u. The frequency shift can be explained in the fringe model by moving fringes in the measurement volume. Frequency shifting presents the advantage in the sense that one can choose by f_{shift} the number of fringes the particle crosses, as fringes and particles are moving relatively to each other.
The frequency shift helps also in giving the burst the correct number of cycles. The burst must be long enough for accurate frequency determination and short enough to avoid multiple validation, that is, the decomposition of one Doppler burst because of noise into several bursts by the interpretation software. In the preliminary measurements, it is observed that a frequency shift of 2 MHz gives best bursts.

3.4.3 Measurement volume

The measurement volume corresponds to the cross-volume of the two laser beams. In ordinary local LDA applications, the size of the measurement volume is small compared to the flow dimensions and local information is obtained. In this research, the measurement volume is slightly larger than the expected liquid film thickness. With the laser equipment used, the smallest measurement volume one can obtain has a length of 260 μm, whereas the mean film height is expected to be in the order of 100 μm according to literature. As a consequence, one can measure velocities in the laminar part of the liquid film as well as the faster moving waves (see figure 3.15). This will be considered below when interpretating the preliminary results.

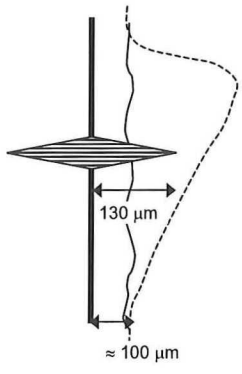

Figure 3.15: Measurement volume (hachured area).

3.4.4 *LDA* set-up

A differential Doppler technique in back-scatter mode is used. A back-scatter method is necessary instead of a forward-scatter one, as the liquid film strongly perturbs the laser beams. A differential Doppler technique is preferred, since it avoids in back-scatter mode the labor-intensive set-up for the alignment of the intersecting leaser beams and the light detector (one laser probe containing the receiver is used).
The laser source is an Argon-Ion laser delivering a power up to 5 W. A TSI IFA 750 processor analyses the signal. A more detailed description of the equipment can be found in [Deelder, 2001].

3.4.5 Preliminary results

The *LDA* experiments are performed on a film of a vertical water-air annular flow, which does not have reached an equilibrium. The measurements are achieved about 60 *cm* above the water entry device. The loop is made of segments, in which no obstacle is inserted.
The vertical axis of the measurement volume is placed on the wall. This location is determined in an empty tube by a maximum response of scattering at the inner wall. When water flows along the wall, this response quasi disappears because of the close refraction indices of water and Perspex compared to air, and the corresponding zero velocity is almost not included in the mean velocity in the measurement volume. With the lenses used, the extent of the measurement volume is larger than the mean film thickness.

In figure 3.16, the mean velocity in the measurement volume, or film, is illustrated as a function of the injected water mass flow for an air velocity of 29 m/s. The measured velocity increases with the water mass flow, but with a reducing slope. Different in the experiments is the frequency shift. Both curves show the same trend. The deviation of maximum 20% probably does not reside in the frequency shift, but in the imprecision of the experiments and the flow non-equilibrium.
In figure 3.17 is added the mean velocity in the measurement volume for an air velocity of 52 m/s. This velocity is smaller than for an air velocity of 29 m/s, except for small water mass flows.

The observed trends can be explained physically. It is expected that more water injected in the tube results in larger films. As the shear in the film decreases with distance from the wall, liquid is dragged upwards with higher velocities further from wall. This increases the mean velocity in the measurement volume.
One observes for constant water mass flows a decrease in the measured velocity with air velocity. This is at first sight contradictory. However, more liquid is entrained at larger air velocities and the liquid film is thinner. The negative impact of the wall shear on the mean velocity in the film is higher. This is not the case at small water mass flows; entrainment does not exist, which results in a higher film velocity compared to smaller air velocities.

The particles moving through the measurement volume differ significantly in velocity. Particles very close to the wall have an almost zero velocity and particles in the disturbance waves have a velocity in the order of 5 m/s. This aspect is observed in the spreading of the velocity spectrum. However, the spectrum includes unphysical velocities as well. The velocities spread from negative ones to very high ones (in the order of $10 - 15$ m/s). Negative velocities are not expected with the air velocities used, since the air flow is believed to drag the liquid film completely upwards. The high measured velocities are also unexplained. Light crosses with difficulty the film interface due to the interface scattering and these high velocities are not expected to correspond to the droplets ones, which in addition are much higher (slightly smaller than the air velocity). These velocities do not correspond to the disturbance waves velocity either, which is smaller by about a factor 2.

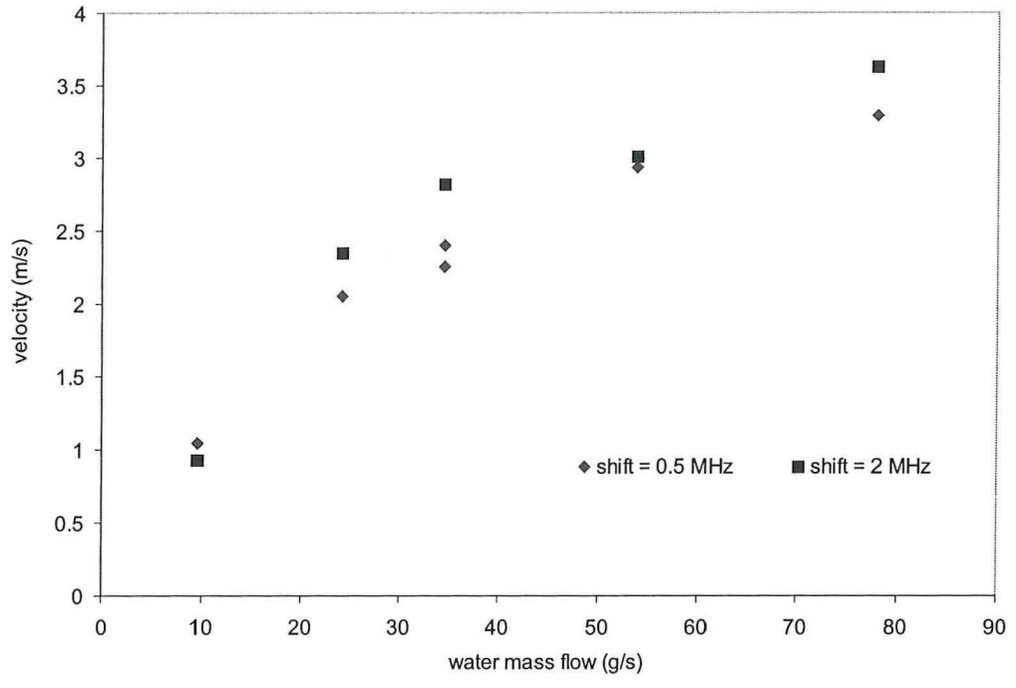

Figure 3.16: Mean film velocity as a function of the water mass flow for an air velocity of 29 m/s.

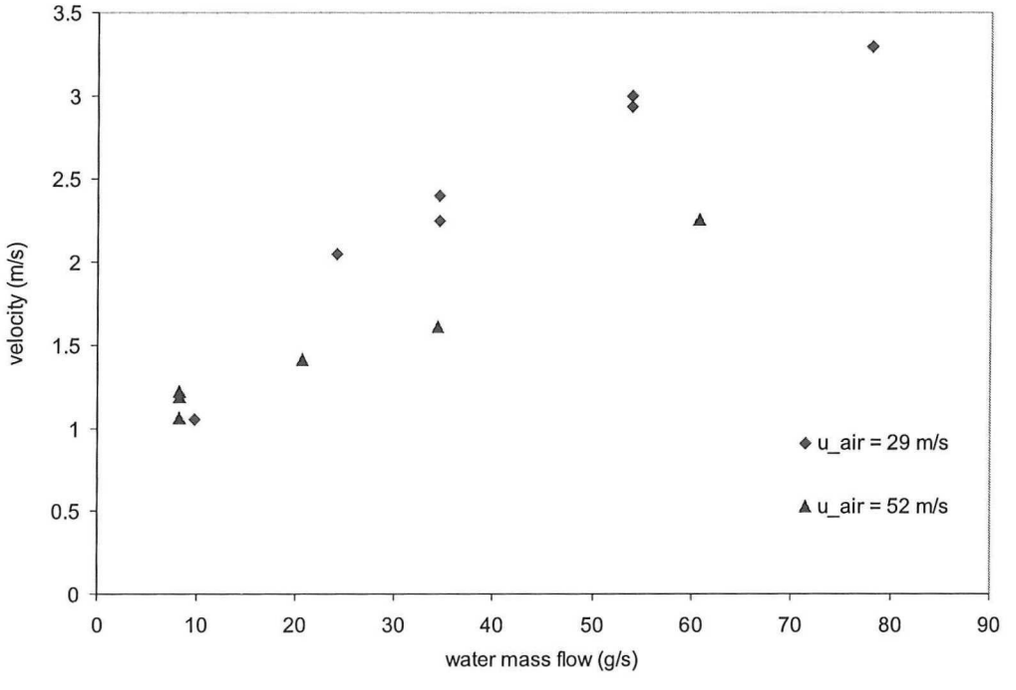

Figure 3.17: Mean film velocity as a function of the water mass flow for different air velocities (29 and 52 m/s).

A further aspect in the spectrum is the approximately Gaussian form, characteristic of random signals.

Although unphysical velocities are contained in the mean, the variation of the averaged velocity with position of the measurement volume in the film is investigated. The measurement volume can be displaced further in the wall (part of the measurement volume in the film covers only part of the substrate film) or further in the tube (part of the measurement volume in the film covers only the interface). Physical results are obtained as well.
When moving the measurement volume progressively into the wall, the measured velocity decreases as well as the data acquisition rate. By moving the measurement volume into the wall, it covers a smaller zone close to the wall, in which the velocities decrease. When moving progressively the measurement volume into the film, one does not observe a clear variation in the mean velocity. A possible reason is that one measures the interfacial velocity (ripple and disturbance waves) averaged in time, as the interface is the main source of scattering. The measured velocity is clearly smaller than the one of the disturbance waves (see chapter 4.5).
Furthermore, when the measurement volume is visually located in the core instead of on the interface, still a velocity is measured. The disturbance waves may cause this signal if the tops pass through the measurement volume. However, these are assumed to move faster than this measured velocity. Droplets as well move significantly faster and the interface blocks a major part of the laser light. This is not explained. Note that the length scales involved in the film are very small compared to the measurement volume.

3.4.6 Conclusion and recommendations

The LDA experiments performed in this research aim to investigate the possibilities of LDA for velocity measurements in a thin liquid film. It can be concluded from the results on the provisory flow-loop:

- Physical trends are shown in the LDA results.
- The interpretation of the measured velocity is not fully clear. One can think especially of the interfacial velocity averaged in time.
- Unphysical velocities are measured, the origin is not established.
- Detailed LDA experiments are necessary to examine and to measure the velocity profile in the film.
- In detailed measurements, an accurate set-up is necessary.

Extensive LDA experiments should take into account the following recommendations.

- One can correlate the averaged velocity obtained by LDA with the interfacial shape obtained experimentally by the conductance probes. Then, in the case the measured velocity corresponds to the interfacial velocity averaged in time, one can obtain the mean velocity of the substrate film.
- An appropriate segment must be used in order to avoid optical aberration. First, the wall thickness of the segment must be as small as possible to avoid a deviation in the direction of the laser beams. Secondly, the surface, on which the laser beams enter the segment, must be flat instead of rounded. Consequently, it is recommended to insert a groove in one segment used for the LDA experiments, as represented in figure 3.18.

- An accurate set-up is necessary for the probe displacement, in which displacements of 10 μm can be measured. Then, LDA measurements will also inform on the film thickness.

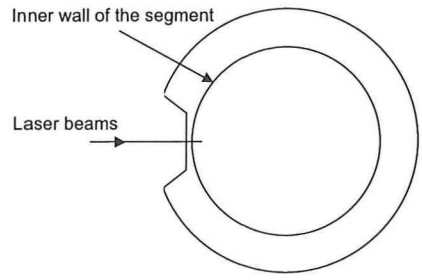

Figure 3.18: Recommended segment to use in LDA experiments.

Chapter 4

Results

In this chapter, the results from experiments are presented. The first two sections present working parameters of the flow-loop used; section 4.1 deals with the equilibrium of the tube flow after the developing length and section 4.2 with the fraction of water existing as droplets in the gas core. Section 4.3 presents the calibration of the conductance probes.
Subsequently are presented the effects of the obstacle on the flow. In section 4.4, the effects of the obstacle on the film thickness are discussed. In sections 4.5 and 4.6, the influence of the obstacle on interfacial phenomena is examined, that is, the disturbance waves velocity and the film shape, respectively.
In section 4.7, the film thickness enhancement results in relation to the CHF are discussed.

4.1 Equilibrium

To obtain interpretable results of the obstacle effects, the annular flow, in which the obstacle is placed, must be in equilibrium. It must be ensured that the 3 m developing length, equivalent to 150 tube diameters, is sufficient to reach the equilibrium. Global film parameters as mean film thickness and disturbance waves velocity are measured by the conductance probes to verify this. The conductance probes are located either 6 and 16 cm or 66 and 76 cm after the developing length. The mean film thickness and the disturbance waves velocity are given as functions of the water mass flow respectively in figure 4.1 for an air velocity of 40 m/s. The observed trends are physical. More water injected in the annular flow leads to a thicker film. In a thicker film, the influence of the wall is less felt at the interface and disturbance waves can travel faster.

The film heights measured at 6 and 16 cm above the developing length are almost constant, the same applies for the couple 66 and 76 cm, but with a deviation of about 10% compared to the preceding couple. The velocity of the disturbance waves velocity is almost constant close and far from the developing length. From figure 4.1, it is considered that the equilibrium is reached after the 3 m developing length. The explanation of the 10% deviation in the mean film thickness is twofold.
First, perturbations may be introduced by the segments connections. The accuracy in the segment diameter is in the order of 10 μm, whereas the film thickness in the order of 150 μm. The transitions between two segments can influence the behavior of the film by either introducing or favoring waves. For this reason, it is decided to measure principally close to the developing length and to use as few as possible segments. Figure 4.2 shows perturbations introduced in the film height at a height

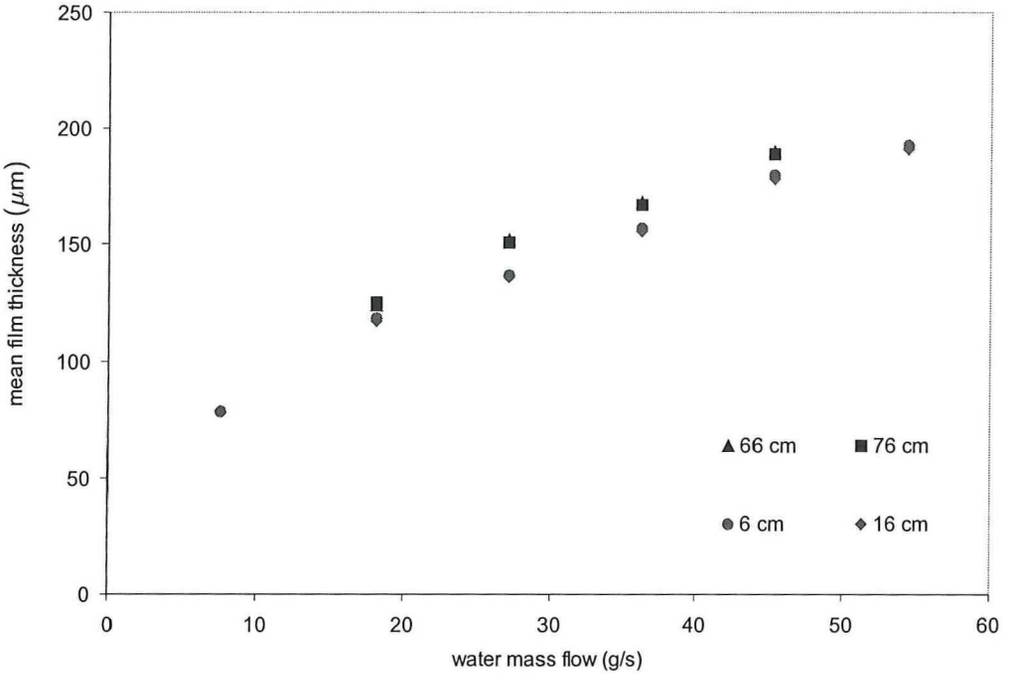

(a) Mean film thickness as a function of the water mass flow. Air velocity of 40 m/s

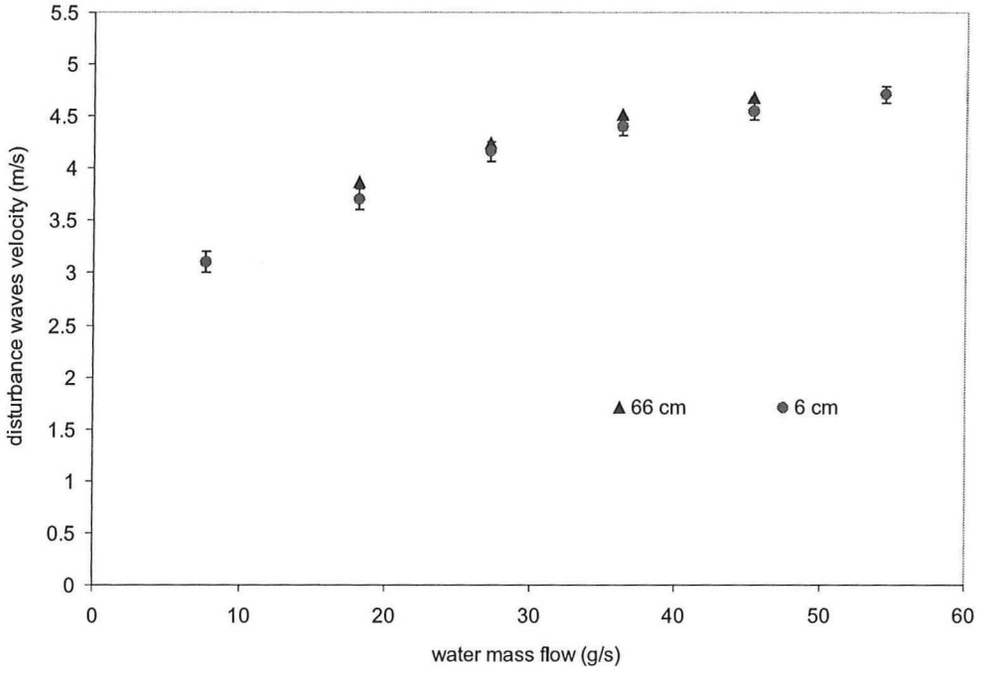

(b) Disturbance waves velocity as a function of the water mass flow. Air velocity of 40 m/s

Figure 4.1: Film parameters at different locations downstream the developing length.

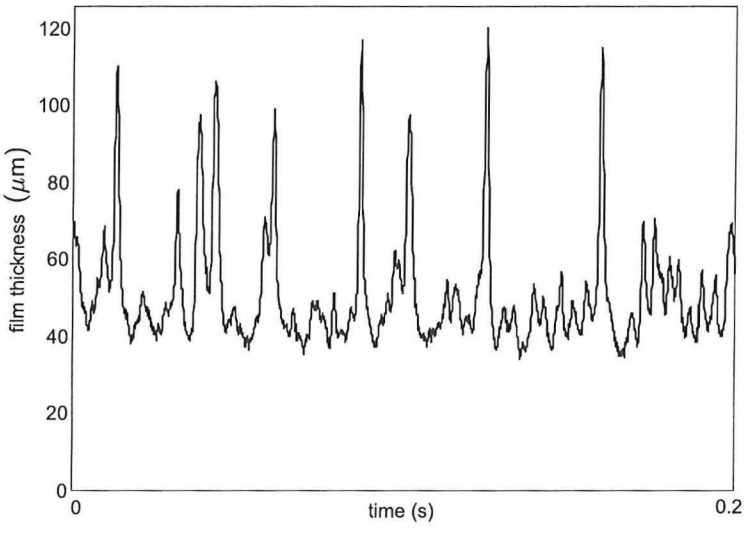

(a) Film height profile 6 cm above the developing length. Water mass flow of 36 g/s and air velocity of 77 m/s

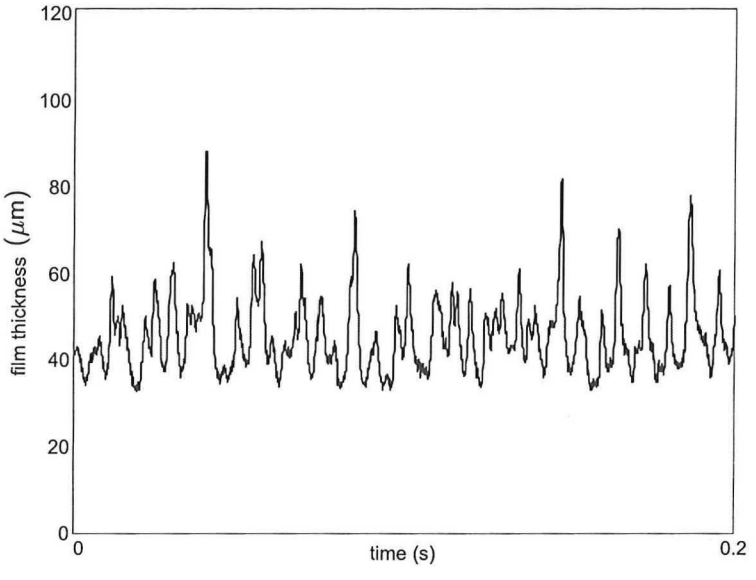

(b) Film height profile 66 cm above the developing length. Water mass flow of 36 g/s and air velocity of 80 m/s

Figure 4.2: Perturbations introduced in the film height profile 66 cm above the developing length compared to 6 cm for a high air velocity.

of 66 cm compared to 6 cm above the developing length. The amplitude of the disturbance waves decreases, whereas the one of the ripple waves increase; as result, the disturbance waves are hardly discernable from the ripple waves. The introduction of waves is also verified on the video-camera when visualizing the transition of the segments.
Secondly, the measurement conditions can have changed between the two measurement series. The changes can possibly reside:

- in different cable resistances due to different electrical connections from hardware to the conductance probes
- in changing water conductivity due to temperature changes or to gas dissolution
- in the atmospheric pressure

The water temperature is controlled before water enters the column, but its temperature can change in the tube by heat exchange with the gas flow, which temperature is uncontrolled. The gases CO_2 and O_2 and other impurities contained in the air flow can dissolve in water. Both aspects can vary the water conductivity. The pressure intervenes by air density in inertia, which governs the interfacial behavior of the film. As the air-water separator is in contact with the atmospheric pressure, the pressure in the test section is equal to the atmospheric pressure plus the pressure drop. Weather conditions can have a large impact on the atmospheric pressure (maximum 5 %) and consequently on the interfacial behavior (personal communication dr. Prasser).

A developing length of 150 diameters is short. In literature is stated that, with other water entry devices, the developing lengths are in the order of 600 diameters. This shows the efficiency of the water entry device used. One can argue that the 10% deviation over 60 cm in the film thickness is still due to non-equilibrium. However, if that is the case, it does not affect the research, as (i) a comparison takes place between the experimental results with and without obstacle and (ii) reproducible conditions are desired and approximately observed over the 26 cm long portion of the test section, where the measurements are performed.

4.2 Entrainment

The liquid film is separated from the air core with the film removal device illustrated in 3.2 and its mass flux is measured by weighting removed water.
The entrained mass fraction, E, defined as the ratio of the entrained mass flow over the injected water mass flow, is illustrated as a function of the injected water mass flow in figure 4.3. No obstacle is inserted.

$$E = \frac{\dot{M}_{LF}}{\dot{M}_L} \tag{4.1}$$

where $\dot{M}_L$ is the injected water mass flow and $\dot{M}_{LF}$ the film mass flow.

Entrainment is far more sensitive to variations in the air velocity than in variations in the water mass flow. It increases with air velocity with a decreasing slope and with the flow of injected water. Too large values are found for the entrained mass fraction for low water mass fluxes. Using the video-camera, the critical water mass flow is measured between 3.3 and 4 g/s for the concerned

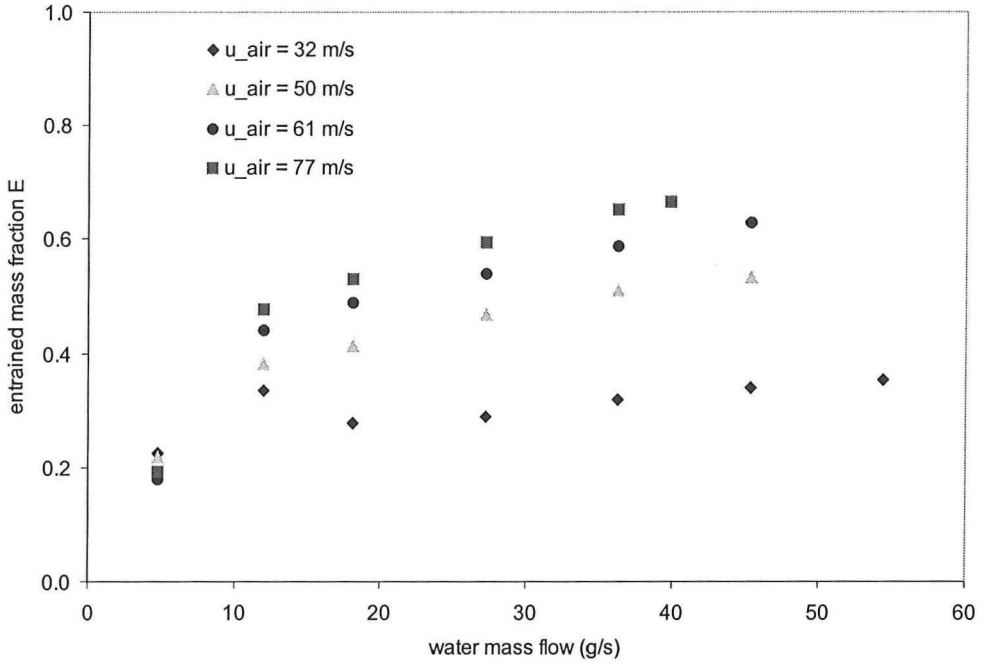

Figure 4.3: Entrained mass fraction as a function of the injected water mass flow for different air velocities.

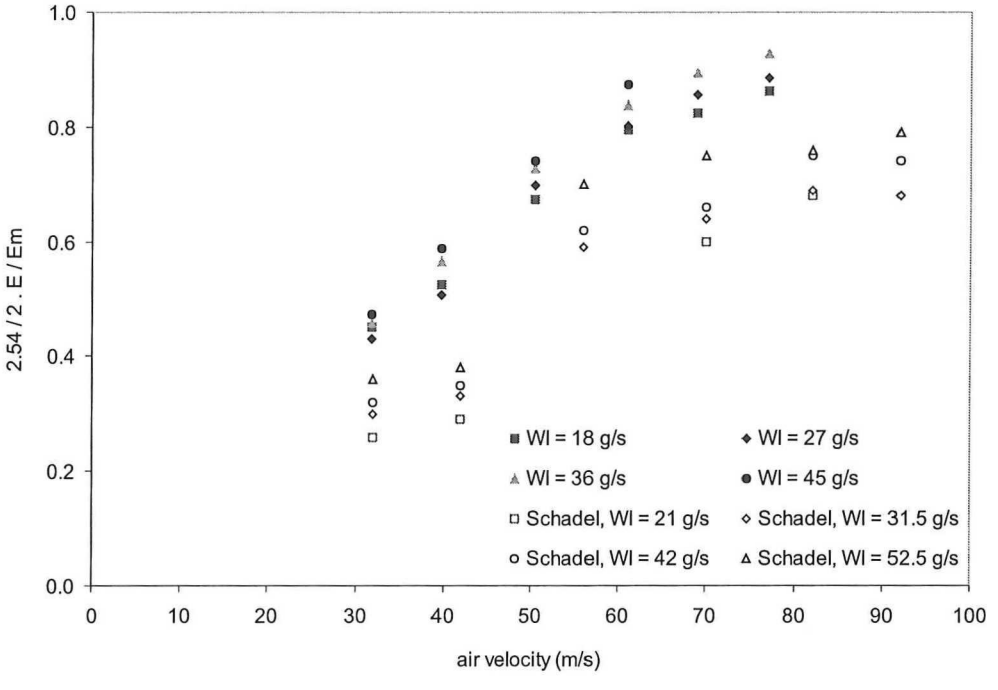

Figure 4.4: E/E_m as a function of the air velocity obtained in this research compared to literature.

velocities (measured as the water mass flow for which the disturbance waves are absent). Nevertheless, at 4.7 g/s, the entrained mass fraction equals approximately 20 %, whereas approximately 0% is expected. The reason probably lies in the water withdrawal device, which cannot discharge correctly the film water. As the device is filled with water, some part of the film is obliged to flow in the core of the film separator. That part is contained in the entrained mass fraction. The outlets of the device must be enlarged or increased in number to remove the film water; perhaps a vacuum pump must be used.

The values of the entrained mass fraction are compared to literature in order to have an idea of the deviation. In figure 4.4 are compared E/E_m, that is, the ratio of the entrained mass fraction E over the maximum amount of entrainment attainable E_m, of this research and of literature. E_m considers that the introduced film in the tube is maximally reduced by entrainment that it flows at the critical mass flow rate:

$$E_m = \frac{\dot{M}_L - \dot{M}_{LFC}}{\dot{M}_L} \tag{4.2}$$

where $\dot{M}_{LFC}$ is the critical film mass flow.
The entrainment measurements in [Schadel et al., 1990] are made using a tube of 2.54 cm diameter. The results obtained in this research must be adapted, according the dimensional relation proposed by [Schadel et al., 1990]:

$$\frac{E}{E_m} \sim D u_G^2 \left(\rho_L \rho_G\right)^{1/2} \tag{4.3}$$

where u_G is the gas velocity, ρ_L the liquid density and ρ_G the gas density.
The experimental $(2.54/2)(E/E_m)$ is compared with E/E_m of literature. The second order polynomial shape of the curves is the same, but with a deviation of 20% between experiments and literature. This overestimation is most likely caused by the incomplete removal of the film as discussed above.

4.3 Calibration

The equipment used for the conductance probes delivers a digital signal (2^{11} bits) proportional to the current signal and consequently to the film thickness. The equipment must be calibrated to assign the ADC units to the corresponding film thickness.

The conductance probes are calibrated by inserting plugs in the probes, leaving gaps of 60, 145, 220, 300, 407, 495 and 615 μm, which are filled with water. The plugs are made of PVC. The 'core' of either droplets laden air flow or PVC is considered insulating in respectively the measurements and the calibration. The insulating property of PVC is verified by placing two electrodes, similar to those in the conductance probes on a PVC plug of the same diameter of the tube. The same response is obtained for the electrodes in contact with air. When inserting that plug in the probe, with water filling the very small gaps in order to make contact between the electrodes and the plug, a slightly larger response is obtained than with air only. This is probably due to water around the plug surface.
One can choose in the program a signal amplification to set the thickness variations over the range of 2048 units. The calibration series performed for the presented measurements is illustrated in figure 4.5.
The calibration curves are linear; the conductance of water in between the electrodes is propor-

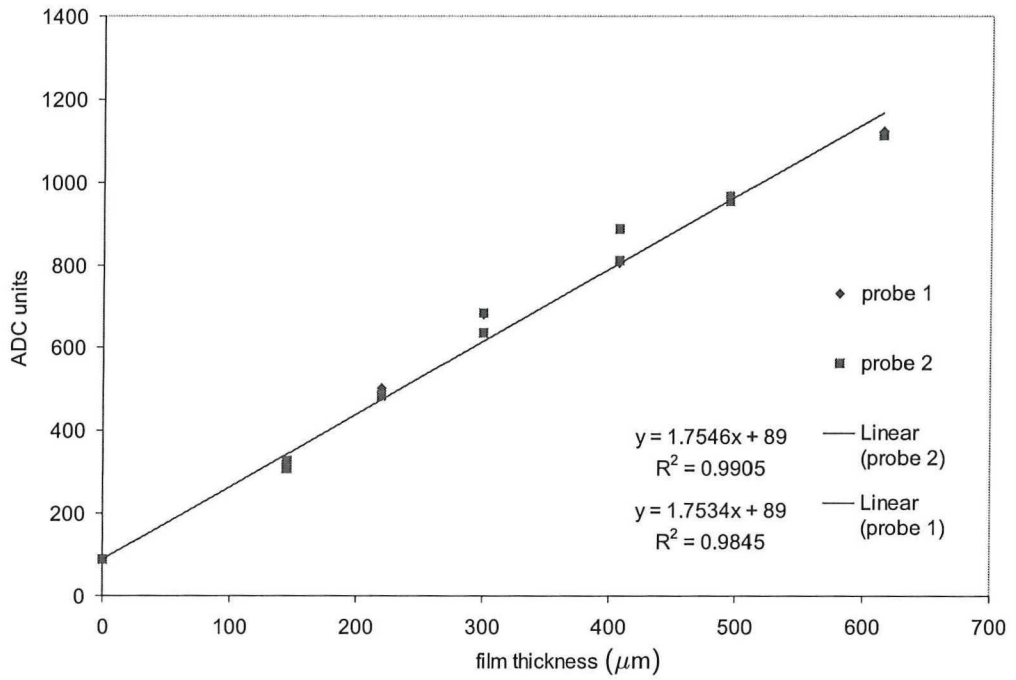

(a) Static calibration for the two probes with an amplification 1-1.

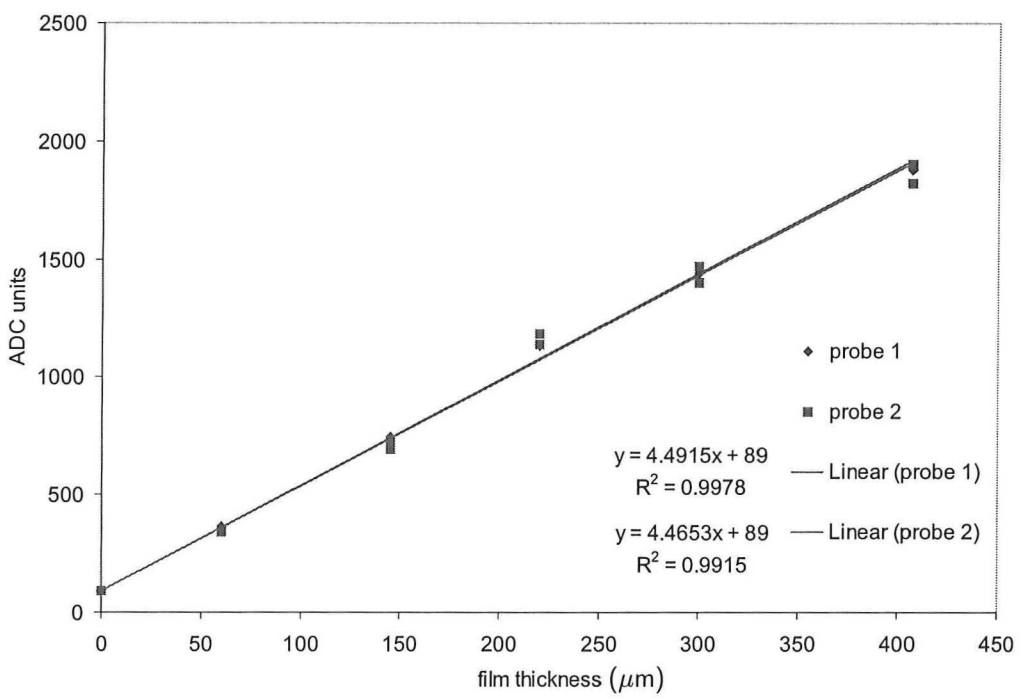

(b) Static calibration for the two probes with an amplification 1-2.

Figure 4.5: Calibration curves for the conductance probes.

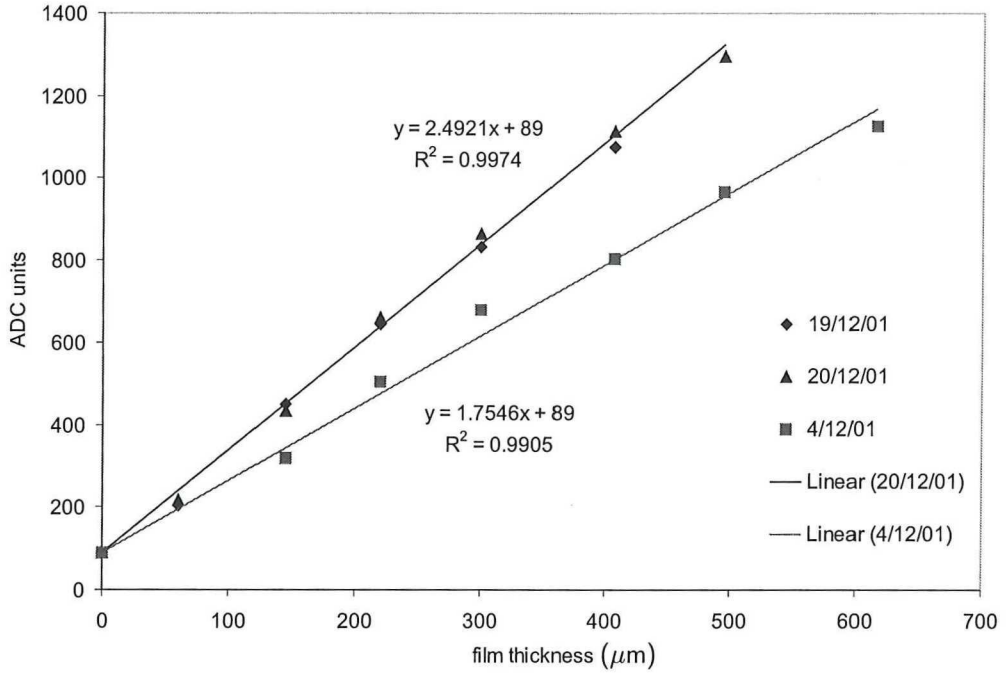

(a) Calibrations on the conductance probe 1 with amplification 1-1.

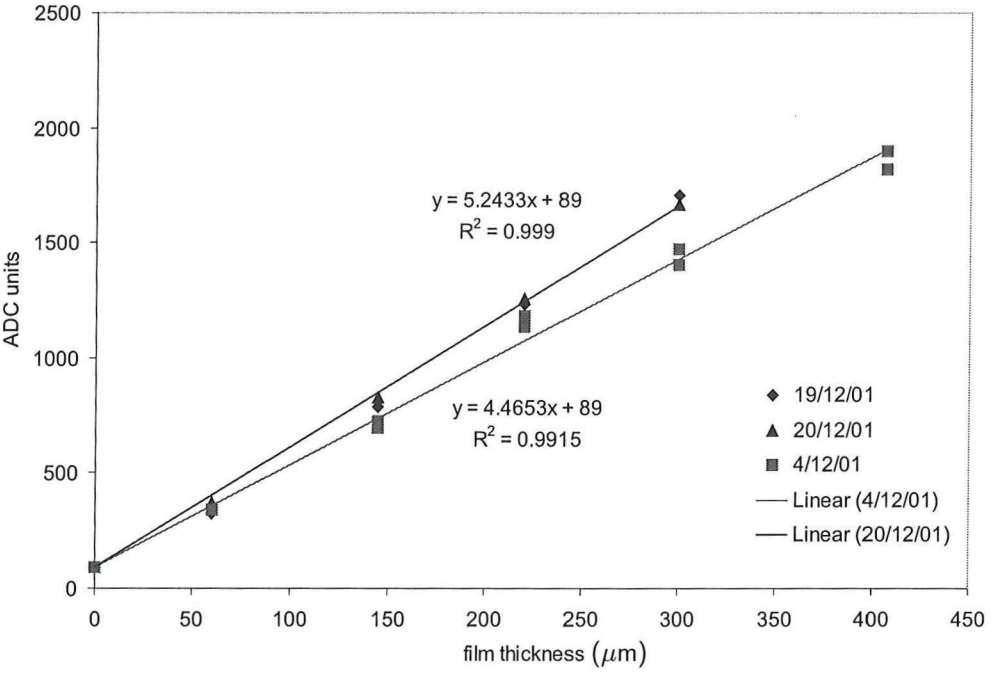

(b) Calibrations on the conductance probe 2 with amplification 1-2.

Figure 4.6: Calibration curves for the conductance probes.

tional to the film thickness. The calibration curves are quasi the same for the two conductance probes; the small differences in the construction of the probes do not influence the response.
Although the number of samples is small, a standard deviation of the calibration measurements to the linear curves is calculated. It is equal to 21 μm for the amplification 1-1 (used for an air velocity of 32 and 40 m/s) and equal to 12 μm for the amplification 1-2 (used for the other air velocities). This is the main source of uncertainty in the film thickness measurements (see the discussion below). 8 to 10 measurements are performed for each calibration curve, which is too small to determine accurately the standard deviation. More measurements were not performed, as (i) initially it was not suspected that the amplitude of the deviation was important compared to the increase in film thickness by the obstacle and (ii) more measurements were later impossible due to the changes in the water conductivity (see below).

The presented measurements have all used the same calibration curves. Note that almost no fresh water is added to the recycle water (only to compensate the small losses in water in the separator and in the pump). The calibration set, the measurements without obstacle and the measurements 6 and 16 cm above the obstacle are performed in 3 consecutive days (04/12/01, 05/12/01, 06/12/01), whereas the measurements 16 and 26 cm above the obstacle are performed 7 days later (12/12/01). Other calibration sets performed 15 and 16 days later (19/12/01 and 20/12/01) have given other calibration curves, as illustrated in figure 4.6.
The slopes of the calibration curves differ considerably. The calibrations are all performed between 20°C and 20.3°C. This shows a variation in the conductivity properties of the recycle water, probably due to dissolution of impurities in the loop-water. Differences in the electrical connections (electrodes-hardware) and the electrical properties of the components in the used equipment could play a role.

4.4 Film thickness

4.4.1 Mean film thickness

The mean film thickness is used first to give a measure of the film behavior, although the film height varies significantly in time. The effects of the flow obstacle on the mean film thickness are illustrated in figures 4.7 and 4.8. The conductance measurements are performed without and with obstacle, 6, 16 (2 times) and 26 cm above the obstacle location in the tube. The obstacle is placed just above the continuous tube serving for developing length.
The mean film thickness behaves as an increasing function of the mass flow of water injected in the tube (see figure 4.7) and as a decreasing function of the air velocity (see figure 4.8).

The mean film thickness is measured without obstacle 6 and 16 cm above the obstacle location in order to supply a reference. Note that no difference is observed between the film thicknesses at 6 and 16 cm.

For the measurements with obstacle inserted, a deviation is observed in the measurements performed at two different moments (06/12/01 and 12/12/01) 16 cm above the obstacle. This deviation is approximately constant for all water mass flows over the region of film heights considered (see figure 4.7). One can think of an offset in the results performed the 12/12/01 simultaneously 16 and 26 cm above the obstacle. Reason to believe this is that, below the critical mass flux, droplets do not exist and droplet deposition cannot occur. Therefore, the mean film thickness must be approximately equal with and without obstacle for water mass flows below the critical one, provided the air flow is the same. In the case of an obstacle inserted, the mean film thickness below

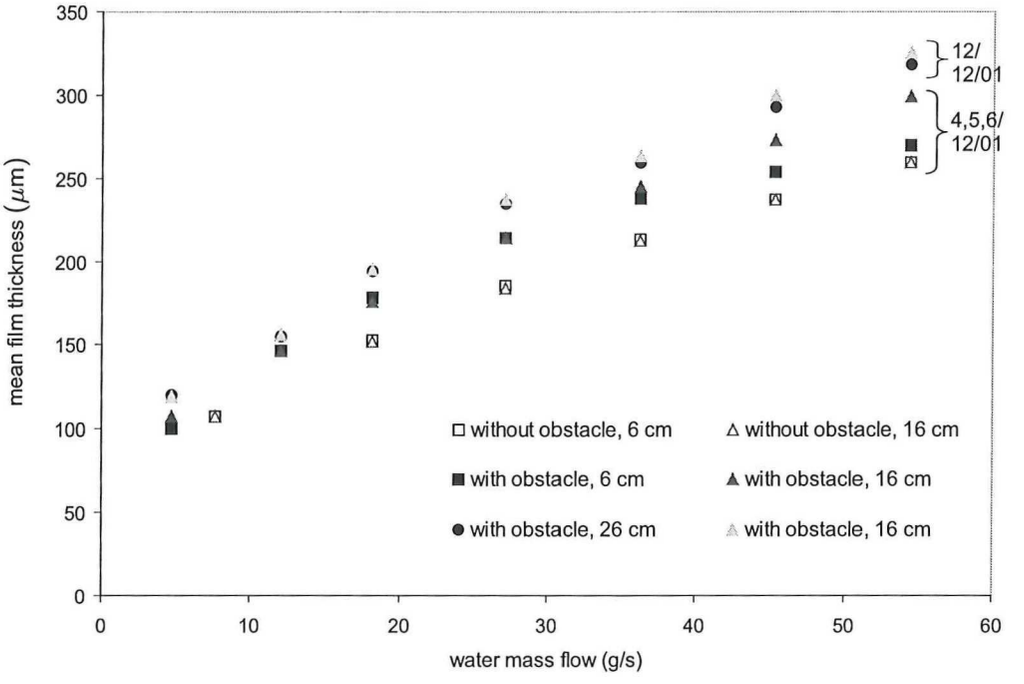

(a) Mean film thickness as a function of the water mass flow. Air velocity of 32 m/s.

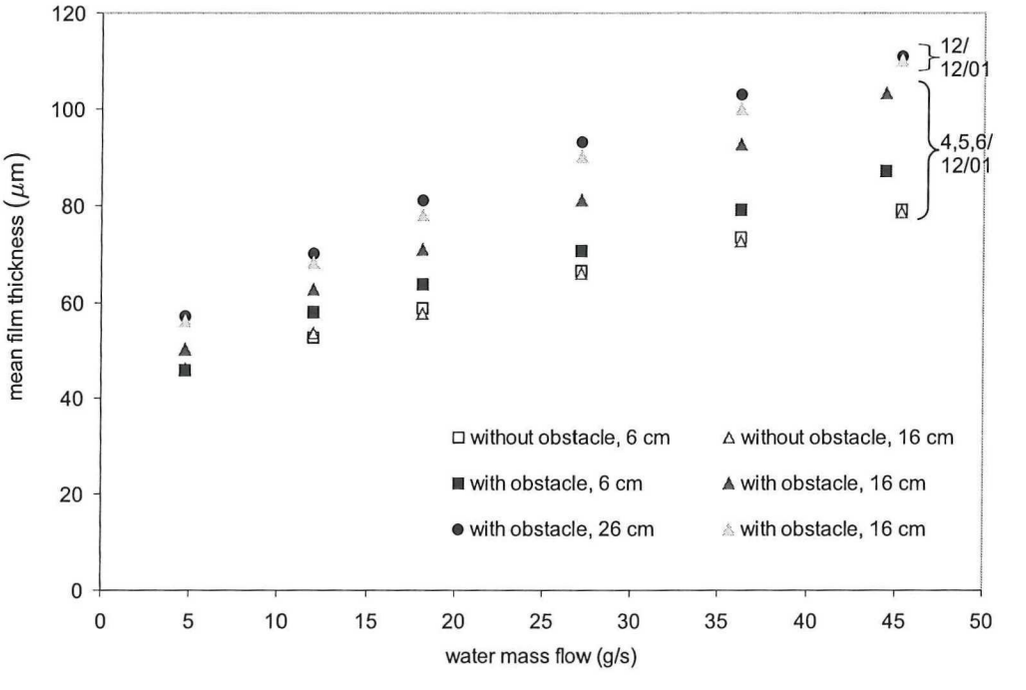

(b) Mean film thickness as a function of the water mass flow. Air velocity of 61 m/s.

Figure 4.7: Effects of the flow obstacle on the mean film thickness. The values measured the 12/12/01 may be subjected to a deviation.

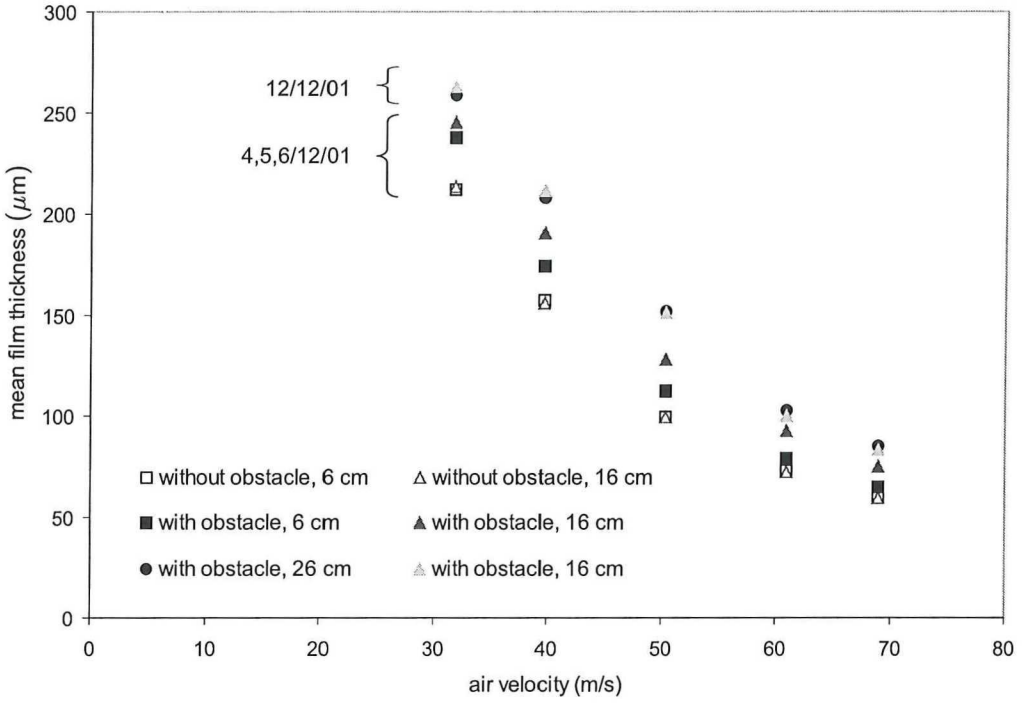

Figure 4.8: Mean film thickness as a function of the air velocity. Water mass flow of 36 g/s. The values measured the 12/12/01 may be subjected to a deviation.

the critical mass flow may possibly be smaller due to the gas flow acceleration induced by the obstacle. The video-camera technique gives a critical water mass flow between 3.3 and 4 g/s. For a water mass flow of 4.7 g/s, the mean film heights measured simultaneously 6 and 16 cm above the obstacle location are approximately equal with and without obstacle, which is not the case for the pair measured simultaneously 16 and 26 cm above the obstacle. A possible reason for offset are the changes in the measurement conditions named before (conductivity, pressure, electrical connections).

The measured film heights are increased by about 15 to 25 % when the flow obstacle is inserted in the flow, the increase depending on the air velocity.
The variation in mean film thickness starts from zero at water mass flows around the critical one and increases progressively with the injected water mass flow. The increase is generally maximum at the highest water mass flow used (except for 6 cm above the obstacle, which is explained at the end of this section), its extent depending on the air velocity. The maximum increase varies from 15 % for low velocities to approximately 25% for high air velocities.
The increase in mean film thickness 6 cm above the obstacle is much smaller than 16 and 26 cm above the obstacle. Considering the offset corrected (by translating the curves of 12/12/01 to superpose the mean film heights 16 cm above the obstacle for mass flows below the critical one), the differences between 16 and 26 cm are minor. Because of lack in precision, it is difficult to pretend that the extent of the increase augments with air velocity, although this is expected and weakly observed (increase at 26 cm seems to be higher than at 16 cm above the obstacle for high air velocities, and the contrary at low air velocities).
In figure 4.8, one clearly sees the decrease in the mean film thickness enhancement 6 cm above the obstacle with air velocity. For higher air velocities, the zone of film thickness enhancement is displaced further downstream the obstacle.
The explanation of the small mean film thickness enhancement directly above the obstacle, which

in addition decreases with air velocity, is twofold. First, the droplets blocked by the obstacles are slung to the wall not radially but following the fast gas flow. Secondly, the obstacle may introduce an acceleration of the droplets laden gas flow near the obstacle, resulting in higher shear and in a smaller film thickness compared to the one in equilibrium and at the same conditions.

The trends observed in figures 4.7 and 4.8 are physical: for water mass flows under the critical one, water is not entrained in the form of droplets and the obstacle has rather no effect on the mean film thickness. For increasing water mass flows above the critical one, disturbance waves appear with increasing frequency, resulting in more entrained droplets in the air core and in potentially more deposited water by forced droplet deposition. In the same way, more droplets are entrained for increasing interfacial shear, that is, for increasing gas velocities, and the amplitude of the mean film thickness enhancement increases with air velocity (see figure 4.7).
The decreasing trend of the mean film thickness for high water mass flows 6 cm above the obstacle location (see figure 4.7) is explained by two points in literature: (i) an increase in the droplet diameter, which decreases the ability of the droplets to follow the gas phase turbulence and hence deposition (diffusion model [Binder and Hanratty, 1991]) and (ii) a dampening of the gas-phase turbulence by droplet-droplet interaction when droplets are in high concentration.

4.4.2 Comparison with literature

The measured mean film heights obtained experimentally by conductance have been compared with empirical correlations of Henstock and Hanratty (1976) and of Asali et al. (1985) in order to validate the measurements.

Both correlations are based on the same approach at high air velocities. Two characteristic lengths are defined for a wavy film entrained by an air flow. These are the mean film thickness $\overline{m}$ and the characteristic friction length $\nu_L/\left(\tau_c/\rho_L\right)^{1/2}$, where $\tau_c = 2/3\tau_w + 1/3\tau_i$ is the characteristic stress in the film (i referring to interface, w to wall) and ν_L the liquid kinematic viscosity. The height of the film is generally related to the mass flow rate in the film; consequently, a dimensionless film thickness, m^+, defined as the ratio of the mean film thickness over the characteristic friction length, is empirically correlated as a function of the Reynolds number of the film, Re_{LF}:

$$m^+ = m^+(Re_{LF}) \tag{4.4}$$

where;

$$Re_{LF} = \frac{4\dot{M}_{LF}}{\mu_L \pi D} \tag{4.5}$$

where μ_L is liquid's viscosity and D the internal diameter of the tube. Henstock and Hanratty (1977) propose the following empirical relationship [Asali et al., 1985]:

$$m^+ = \left(0.420 \cdot Re_{LF}^{1.25} + 2.796 \cdot 10^{-4} \cdot Re_{LF}^{2.25}\right)^{0.4} \tag{4.6}$$

whereas Asali et al. (1985) found better agreement for vertical upflow with entrainment and for tubes diameters larger than 2 cm (mainly 4.2 cm) with the equation [Asali et al., 1985]:

$$m^+ = 0.19 \cdot Re_{LF}^{0.7} \tag{4.7}$$

For a first prediction, the relationship of Asali et al. (1985) is used, the characteristic stress taken

equal to the wall stress, based on the gas flow only, because of the very thin film with high air velocities:

$$\frac{\tau_c}{\rho_G u_G^2} = 0.023 \cdot Re_G^{-0.2} \tag{4.8}$$

The second prediction used the relationships of Henstock and Hanratty (1976) with their following relations for vertical upflows:

$$\frac{\overline{m}}{D} = \frac{6.59F}{(f_i/f_s)^{1/2}} \tag{4.9}$$

$$\frac{f_i}{f_s} - 1 = 1.400 \cdot F \tag{4.10}$$

$$f_s = 0.046 \cdot Re_G^{-0.2} \tag{4.11}$$

$$F = \frac{m^+}{Re_G^{0.9}} \frac{\nu_L}{\nu_G} \left(\frac{\rho_L}{\rho_G}\right)^{1/2} \tag{4.12}$$

where f_i and f_s are the friction factors of respectively the interface and wall, F a flow factor and ν_G the gas kinematic viscosity.
Both predictions differ significantly from the measured mean film heights by a factor 2 to 3. This large deviation is not understood. The calibration makes the measurements relatively reliable. The variation can come from correlations, which are derived empirically for tubes diameters significantly larger than the one used in this research. Correlations for smaller tubes must be found in literature in order to make proper comparisons. The film mass flow rate, needed in the prediction, is derived experimentally by the entrainment measurements. The film flow rate is expected to underestimate the film flow rate by about 20%, as explained above. However, this results in an increase of the difference instead of a decrease. The static calibration is not believed to introduce errors in the dynamic measurements; all the more since literature studies employ as well a similar static calibration.

4.4.3 Maximum film height

The maximum film height corresponds to the mean maximum height of the disturbance waves over the time series. It is illustrated as a function of the water mass flow in figure 4.9. The maximum film height increases with water mass flow. The deviation is again present for the second series of measurement 16 cm above the obstacle.

The effects of the flow obstacle on the maximum film height are unclear. The variation in the maximum height with obstacle compared to that without an obstacle is generally smaller than the standard deviation, which is calculated over the time series.
The enhancement of the mean film thickness is small compared to the maximum height of the disturbance waves and this explains the small variation in the maximum height. One can conclude that the increase in the mean film thickness by the obstacle is not due to an increase in the height of the disturbance waves only, but to an increase of the thickness of the entire film.

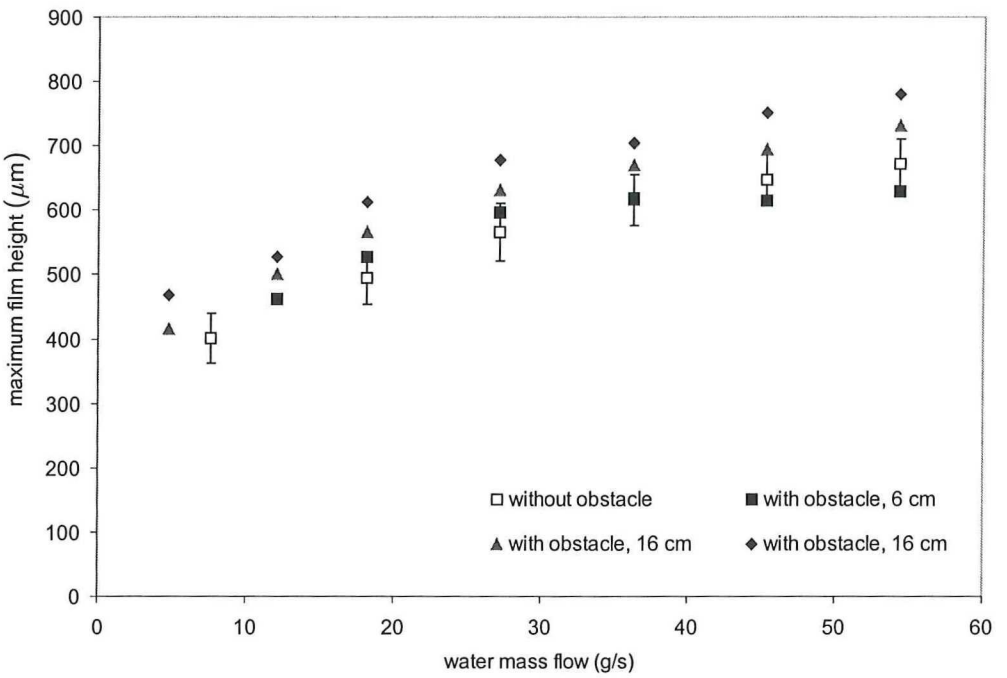

(a) Maximum film height as a function of the water mass flow. Air velocity of 32 m/s.

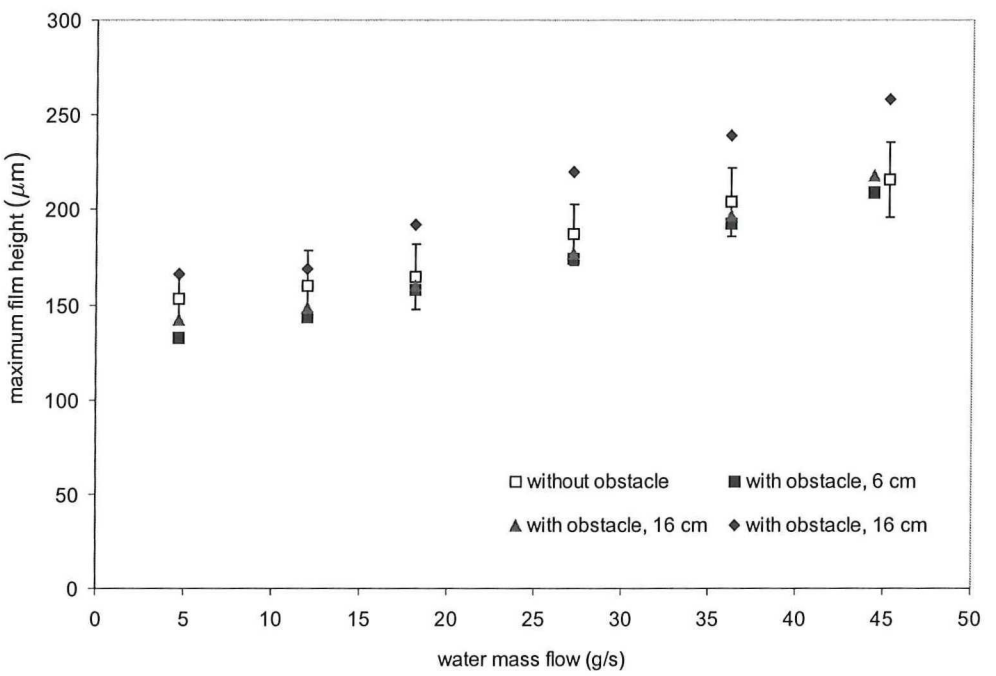

(b) Maximum film height as a function of the water mass flow. Air velocity of 61 m/s.

Figure 4.9: Effects of the flow obstacle on the maximum film height. The diamonds (values measured the 12/12/01) may be subjected to a deviation.

Note that the maximum film height around the critical water mass flux (4.7 g/s) is questionable, as the waves are small in number.

4.4.4 Substrate film thickness

The substrate film is the layer, on which the disturbance and ripple waves move. This layer is exposed to forced droplet deposition between the successive disturbance waves. It is aimed to obtain the increase in height of this film substrate.
It is difficult to determine objectively the thickness of the film substrate if one looks to the time series, especially for higher air velocities and for larger distances from the obstacle. It is decided to assign the film substrate thickness to the mean value of the film heights under a threshold equal to the mean film thickness. All values exceeding the mean film thickness are filtered out (see figure 4.11).

The resulting thickness is presented in figure 4.10 as a function of the injected water mass flow. The substrate film thickness is increased when the obstacle is inserted in the flow. The same observations can be made as for the mean film thickness. The obstacle influences the substrate height of the entire film. The increase in the substrate film thickness is noticeable for water mass fluxes significantly higher than the critical one (higher than approximately 15 g/s depending on the air velocity), the increase being larger than once the standard deviation measured over the corresponding time series. However, the increase in the substrate film thickness is never significantly higher, which leads to discussion and a necessity of a sensitivity analysis of the measurements on the results.

4.4.5 Discussion

Errors in the film thickness response are possibly introduced because of:

- a uncertainty relative to the calibration curves
- a non-constant mean film thickness due to changes in the flow-loop instrumentations (ex: rotameters) during the time series
- a drift in the electrical components inside the conductance probes equipment

The latter point is not tested. Measuring the signal obtained for a set of electrical resistances over a long period can test this. However, such a variation is not believed to occur, since the equipment is never shut down and the components have reached a steady temperature. The ADC converter has a discretization error of half a unit, which is negligible.
The real mean film thickness may vary over the 180 s time series, because of a 'drift' of the equipment (among others pump, flow meters, measurement equipment). The standard deviation on the mean film thickness calculated for 504 sections of the 180 s time series is equal to 1 μm. Consequently, this aspect does not affect the reliability of the measurements.
Uncertainty resides in the real thickness and the thickness given by the calibrated equipment. It is assumed that the deviation in the measurements is of the same order as the one in the calibration measurements. The latter is given by the deviation of the measured points with the calibration curve. The standard deviation in the calibration is equal to 21 μm for the amplification 1-1 (used for an air velocity of 32 and 40 m/s) and equal to 12 μm for the amplification 1-2 (used for the

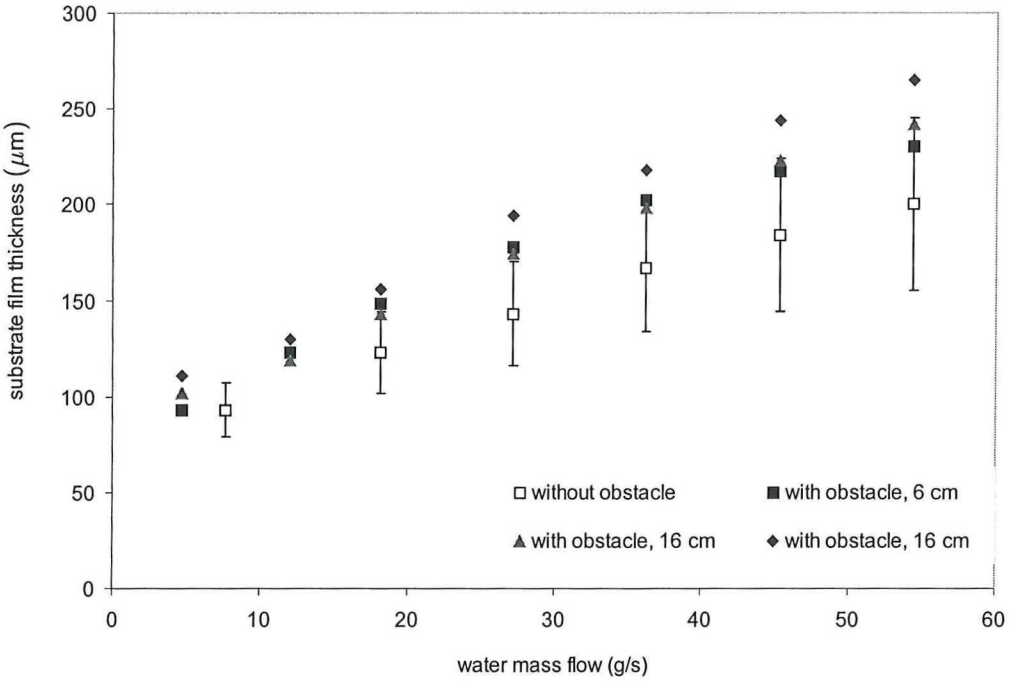

(a) Substrate film height as a function of the water mass flow. Air velocity of 32 m/s.

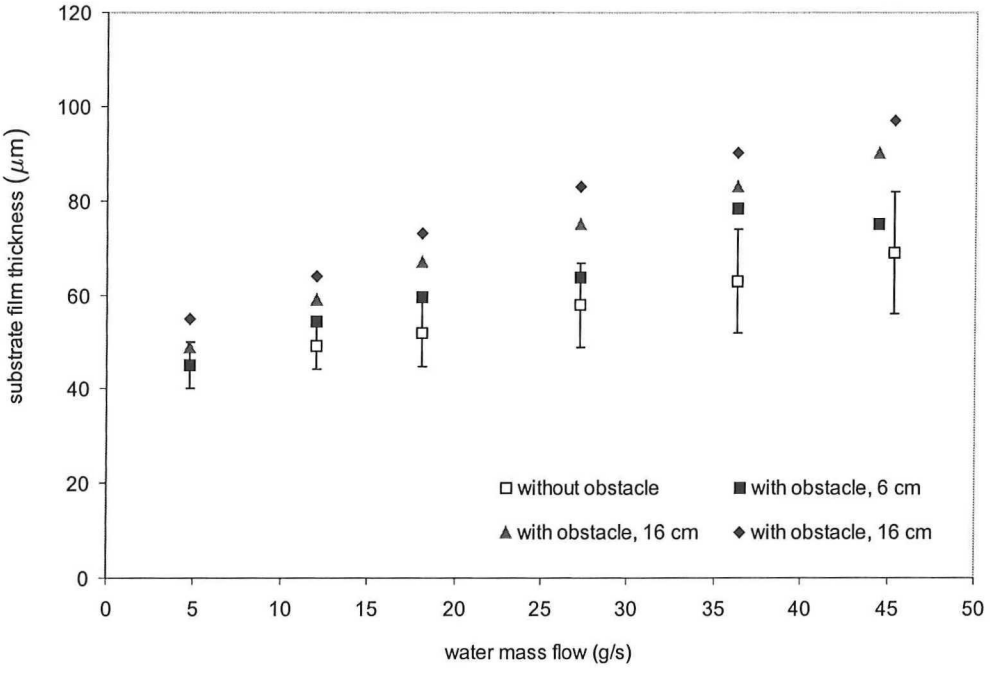

(b) Substrate film thickness as a function of the water mass flow. Air velocity of 61 m/s.

Figure 4.10: Effects of the flow obstacle on the substrate film thickness. The diamonds (values measured the 12/12/01) may be subjected to a deviation.

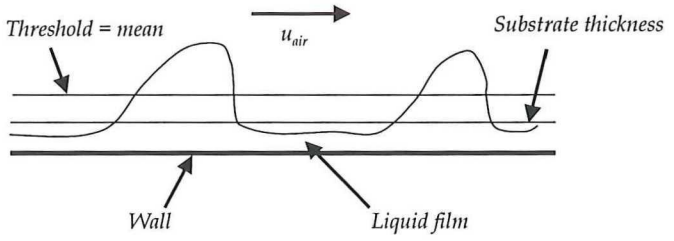

Figure 4.11: Determination of the film substrate thickness.

other air velocities). Note that the calibration is made for a too small number of samples; the values indicate just the order of the standard deviation. Moreover, the measured points in the calibration are mean values, whereas the values are varying with 1 μm around the mean. Both standard deviations are accounted for. Note that the diameter of the plugs is measured after their fabrication. The diameter used in the calibration is assumed to be exact, although a maximum deviation of 5 μm is possible (resolution of the measuring rod).
The errors in the film thickness measurements are summarized in table 4.1.

Table 4.1: Standard deviation in the film thickness measurement.

source of deviation	amplification 1-1	amplification 1-2
deviation of points to calibration curve	22 μm	13 μm
mean thickness deviation in time series	1 μm	1 μm
drift in electrical equipment	negligible	negligible
standard deviation	14 μm	23 μm

One must be warned with the verity of the obstacle effects, as the enhancement of the film thickness by the obstacle is not significant compared to the possible measurements error, especially for measurements with high air velocities (use of amplification 1-2).

Later measurement tests with conductance probes have given similar trends, but slightly translated. These measurements are performed about two weeks later in different conditions (pressure, air temperature, conductivity). The measurements are performed at the same day as the calibration for the measurements; the translation shows that not only changes in water conductivity cause a variation in film thickness. Note from figure 4.6 that the new set of calibration curves vary significantly compared to the other calibration set, showing the variation in water conductivity with time.
It appears that the pressure can play a significant role in the interfacial behavior. This is notably observed when shutting the gas outlet, clearly different results in the mean film thickness are observed. The role of the pressure must be accounted for in later measurements.

The spokes perturb visually the film; a trace of a thinner film is observed behind each spoke. However, this trace disappears rapidly after about 5 cm. The spokes do not influence the conductance measurements above the obstacle. If still a small influence exists, it is almost averaged out since the conductance probes average the response circumferentially.

4.5 Disturbance waves velocity

The time series of the film thickness obtained by two distinct conductance probes separated by 10 cm are cross-correlated to obtain the velocity of the axially coherent disturbance waves. More specifically, the time series 180 s long is cut in smaller time series of approximately 0.35 s, on which the cross-correlation method is applied. A biased method is used; however, the bias is very small since the displacement in the curve is 1/25 of the sections of the time series.

The velocity of the disturbance waves with and without obstacle is represented in figure 4.12 as a function of the water mass flow entering the tube for constant air velocity. Measured velocity is the velocity between 6 and 16 cm and between 16 and 26 cm above the obstacle location in the tube.
The trends encountered are physical: the velocity of the disturbance waves increases slowly with water mass flow and with air velocity. The obstacle has rather no effect on the disturbance waves velocity. The disturbance waves are essentially an interfacial phenomena depending on the air velocity and travel on the substrate film.

These trends are as well encountered in literature [Azzopardi, 1986] and the results agree fairly well with literature, falling in the zone of results of other researches.

The experimental results for the velocity of the disturbance waves obtained with the conductance probes and the video-camera are compared in figure 4.13. No obstacle is inserted for these measurements.
The velocities obtained with the video-camera resemble those obtained with the conductance probes. The deviation relative to the smooth trend is more pronounced with the video-camera technique, which has also a significantly larger standard deviation (in the order of 0.5 to 1 m/s). Nevertheless, it can be concluded that the results obtained with the video-camera confirm those obtained with the conductance probes, as far as the velocities are involved.

4.6 Film shape

As the velocity of the disturbance waves is almost not affected by the obstacle, one is interested to study the influence of the obstacle on other interfacial parameters as the interfacial shape of the film. The power spectrum of the signal of the conductance probes must be known in order to inform on the frequencies of the waves traveling on the film.

The power spectrum is obtained as follows. The time signal of 180 s long is cut into N records. On each record, a fast Fourier transformation is applied giving a scaled power spectrum. Averaging the power spectra of all records leads to the final power spectrum of the time signal. The advantage of this procedure is a lower standard deviation, σ, for a higher number of records, N.

$$\sigma \sim \frac{1}{\sqrt{N}} \tag{4.13}$$

Nevertheless, one must take care that the records contain sufficient points for an accurate power spectrum determination of each record. Furthermore, a window is applied on each record to avoid high-energy steps at the beginning and end of each record. The window attaches a weight on the discrete points in each record; the weight of the points at the beginning and end of each record being low compared to the rest of the points.

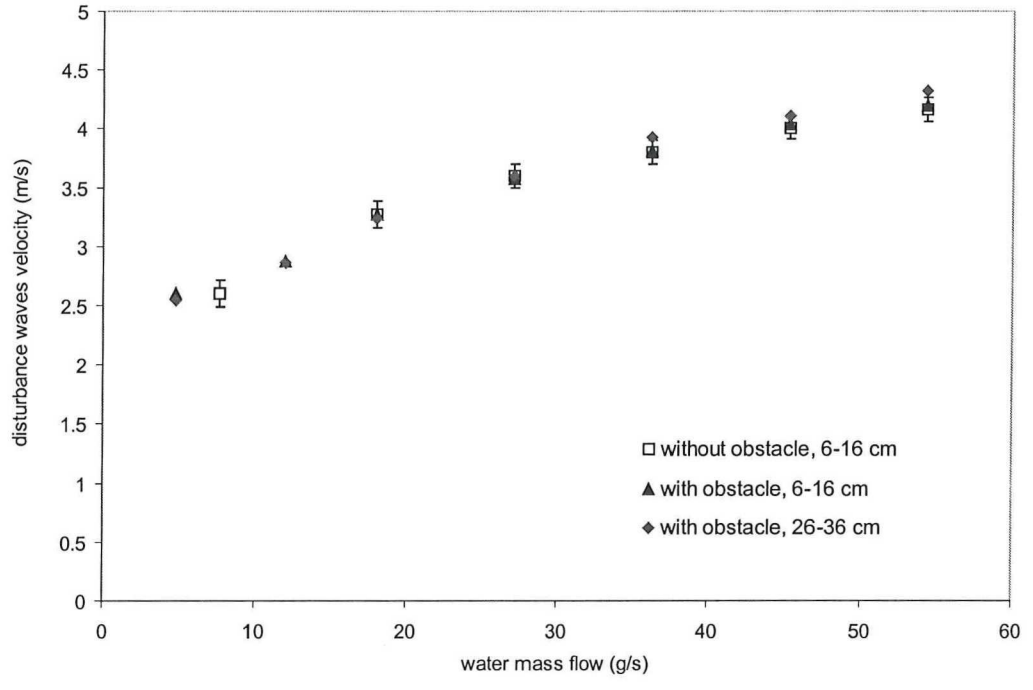

(a) Disturbance waves velocity as a function of the water mass flow. Air velocity of 32 m/s.

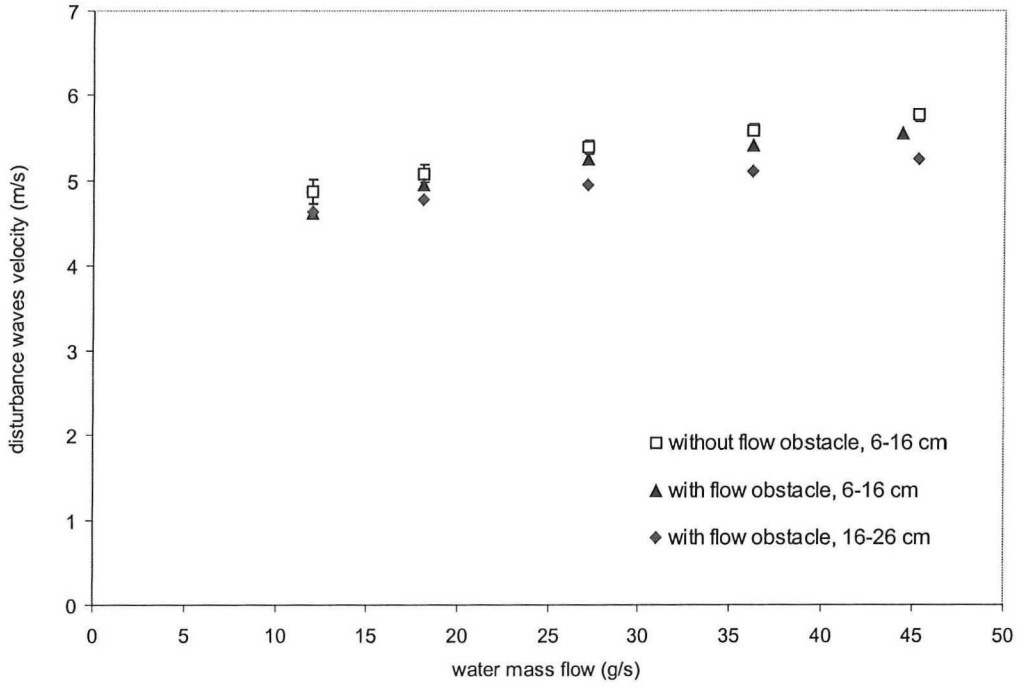

(b) Disturbance waves velocity as a function of water mass flow. Air velocity of 61 m/s.

Figure 4.12: Effects of the flow obstacle on the disturbance waves velocity.

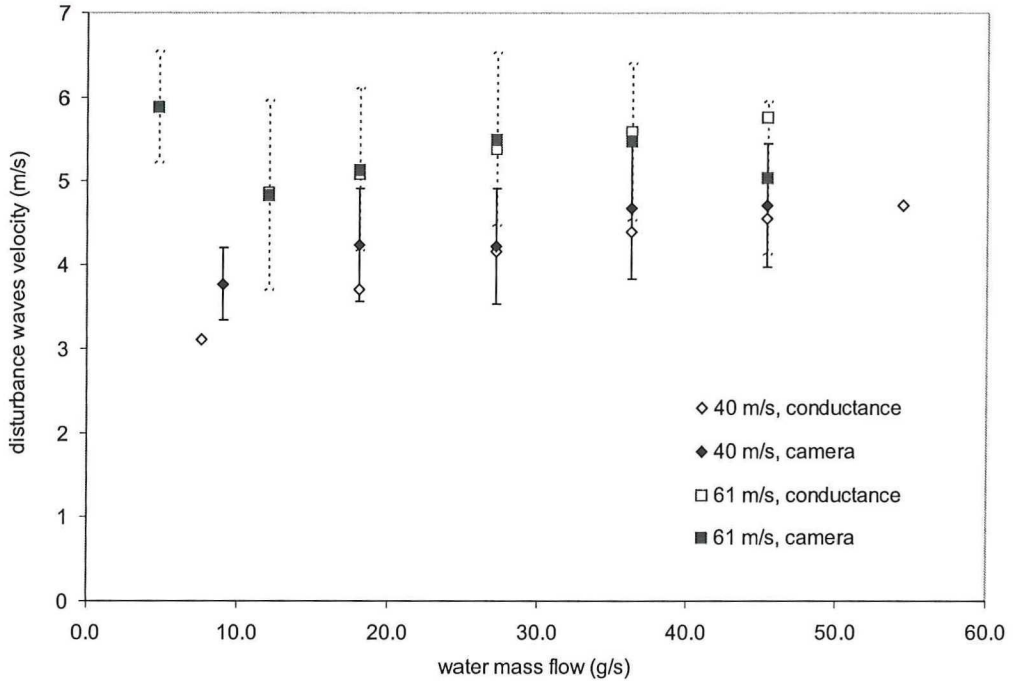

Figure 4.13: Comparison of the results obtained with the conductance probes and the video-camera. Air velocities of 40 and 61 m/s.

In this research, the time signal is cut into 77 records, on which a Hanning window is applied. The standard deviation is 11%.

The power spectra in logarithmic scale, illustrated in figure 4.14, are typical ones and are obtained for an air velocity of 32 m/s and a water mass flow of 27 g/s with and without obstacle.
The peak in the power spectrum corresponds to the fundamental frequency of the disturbance waves (the passage frequency of the maximum film heights), f_o. This is verified in the time series by measuring the time distance between two successive disturbance waves tops. The width in the peak corresponds more or less to the standard deviation in the time distance between successive disturbance waves. Comparison with literature is difficult; the wave frequency decreases with increasing tube diameter and most researches use larger tubes [Azzopardi, 1986]. Nevertheless, the order of magnitude seems to be fair; the results with tubes larger by a factor 1.6 are smaller by a factor of about 2.

From the figure 4.14, it can be concluded that the obstacle does not influence the global interfacial shape of the film. The difference lies only in the energy contained in the amplitude of the peak in the power spectrum. Nevertheless, the obstacle is expected to induce high-frequency fluctuations in the film. The linear decrease in the power spectrum in logarithmic scale can refer to a low-pass filter with a cut-off frequency of around 50 Hz. From figure 4.14, one can note a linear decrease of slope 180 to 200 dB per 100 Hz.

The geometrical configuration of the conductance probe introduces a low-pass filter at 800 Hz approximately and averages out higher-frequency fluctuations on the disturbance waves (explaining the smooth profile of the disturbance waves in the time series). The disturbance waves travel at approximately 5 m/s between the electrodes separated by 6 mm, giving a characteristic frequency of 833 Hz. On the power spectrum appears indeed a change in the slope around 800 Hz, but this does not explain the low-pass filter at 50 Hz.

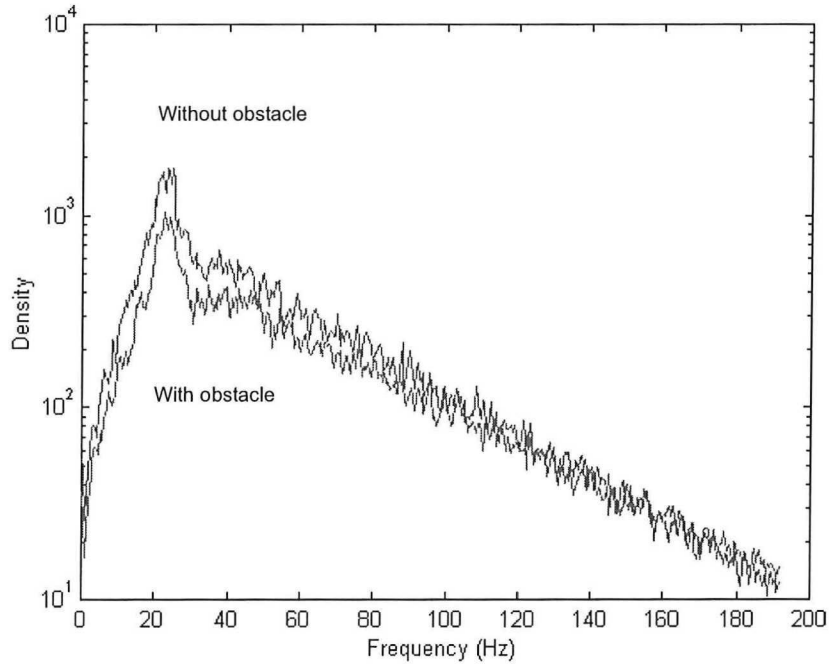

Figure 4.14: Power spectrum obtained for an air velocity of 32 m/s and a water mass flow of 27 g/s.

One can propose two possible explanations for the exponential decrease in the power spectrum, which must be examined. Both are based on a schematic representation of the waves as a periodic square wave signal, $x(t)$, defined over one fundamental period, T, as:

$$x(t) = \begin{cases} 1 & |t| < \tau \\ 0 & \tau < |t| < T/2 \end{cases} \tag{4.14}$$

Corresponding coefficients in the Fourier series a_k are, with ω_o the pulsation equal to $2\pi f_o$:

$$a_o = \frac{2\tau}{T} \qquad a_k = \frac{\sin k\omega_o \tau}{k\pi} \qquad k \neq 0 \tag{4.15}$$

The first possible reason is that the harmonics of the Fourier transforms rapidly decrease in the form of an exponential function. In figure 4.15.a and 4.15.b, the power spectrum of the harmonics of the Fourier series are plotted for a water mass flow of 27 g/s and an air velocity of 32 m/s. Possible values of 0.006 s or 0.009 s are taken for τ in the calculation of both power spectrums from the Fourier coefficients, as can be noted from the time series in figure 4.16 corresponding to the power spectrum in figure 4.14. However, from the figures 4.15, it can be concluded that the harmonics for a given value of τ do not decrease rapidly in a exponential form, but instead in appreciable bumps.

Secondly, the "real" signal contains disturbance waves of different durations (different τ for T constant) and also of different fundamental frequencies (different T). These signals are added. The power spectrum becomes more complex for frequencies higher than the fundamental one; the summation of all signals with different values of τ may give the exponential decrease observed in the power spectrum of figure 4.14.
This filter has to be examined further. Note that it is not due to the use of windows, which can cause high-energy steps at a calculated frequency of 0.4 Hz.

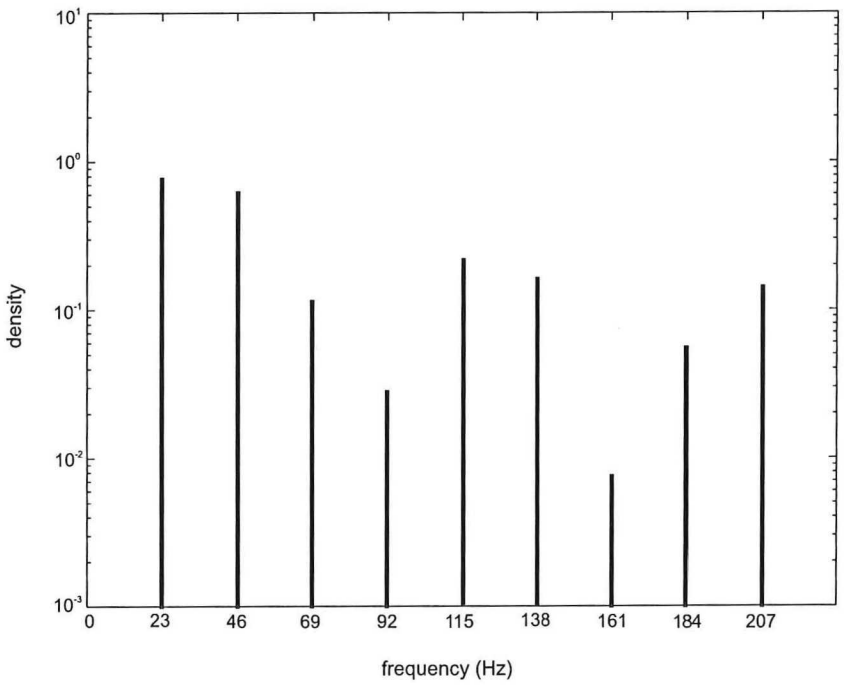

(a) Power spectrum of the harmonics of the Fourier series, τ taken equal to 0.006 s.

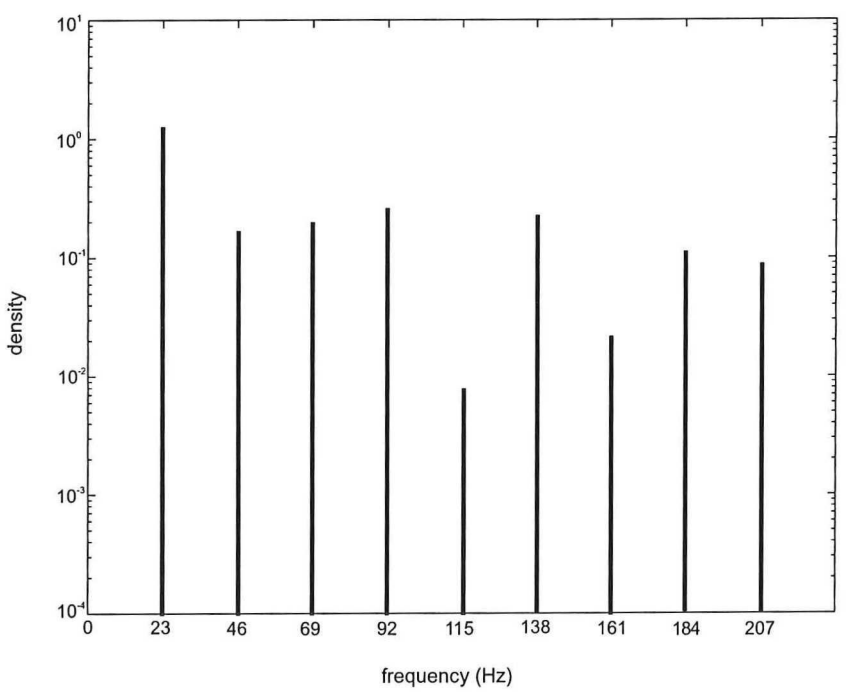

(b) Power spectrum of the harmonics of the Fourier series, τ taken equal to 0.009 s.

Figure 4.15: Possible explanation for the cut-off filter at 50 Hz.

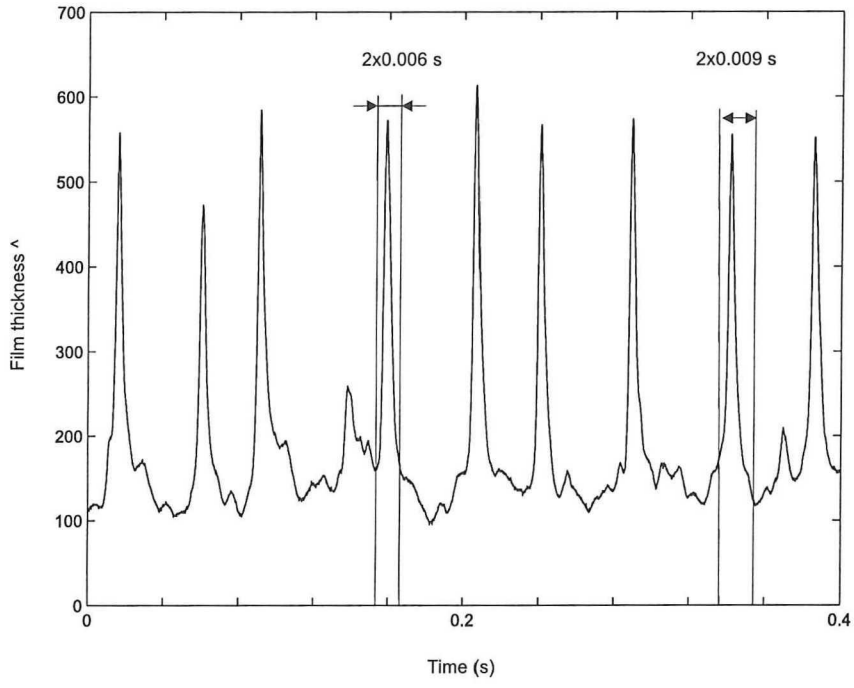

Figure 4.16: Time series showing the time distance between two successive disturbance waves. Air velocity of 32 m/s and water mass flow of 27 g/s.

Nevertheless, the power spectrum informs on the variation of the fundamental frequency of the disturbance waves with water mass flow and with air velocity (see figure 4.17).
Figure 4.17 shows an increase in the wave frequency with water mass flow and air velocity, as is expected physically. Note that the peak due to the fundamental frequency disappears in the filter for high air velocities, showing the necessity of eliminating the filter.

4.7 Thickness enhancement in relation to the CHF

Consider the equilibrium annular flow, in which the obstacle is inserted. The increase in the droplet deposition rates leads to a thicker film compared to the one in absence of the obstacle. One can derive a mass balance over the distance Δz between the obstacle location and one of the measurements points (6, 16 and 26 cm above the obstacle), with assuming a linear increase between these points, a constant entrainment rate and a constant mean film velocity, $\overline{u}$, compared to the equilibrium (because of the small thickness increase). Then, one finds:

$$\pi(D - \overline{m})\Delta z(R_{D,obs} - R_D) = \rho_L \frac{\Delta V}{\Delta t} \tag{4.16}$$

where R_D and $R_{D,obs}$ correspond respectively to the droplet deposition rates without and with obstacle, $\overline{m}$ to the mean film thickness without, and $\Delta V/\Delta t$ to the geometrical increase in volume due to extra droplet deposition (calculated as cylinder-truncated cone):

$$\Delta V = \Delta z \pi \left(\frac{\overline{m}^2}{6} - \frac{\overline{m}_{obs}^2}{12} - \frac{\overline{m} \cdot \overline{m}_{obs}}{12} + \frac{D}{4}(\overline{m}_{obs} - \overline{m}) \right) \tag{4.17}$$

where $\overline{m}_{obs}$ is the mean film thickness with obstacle. Then, one obtains for the increase in the

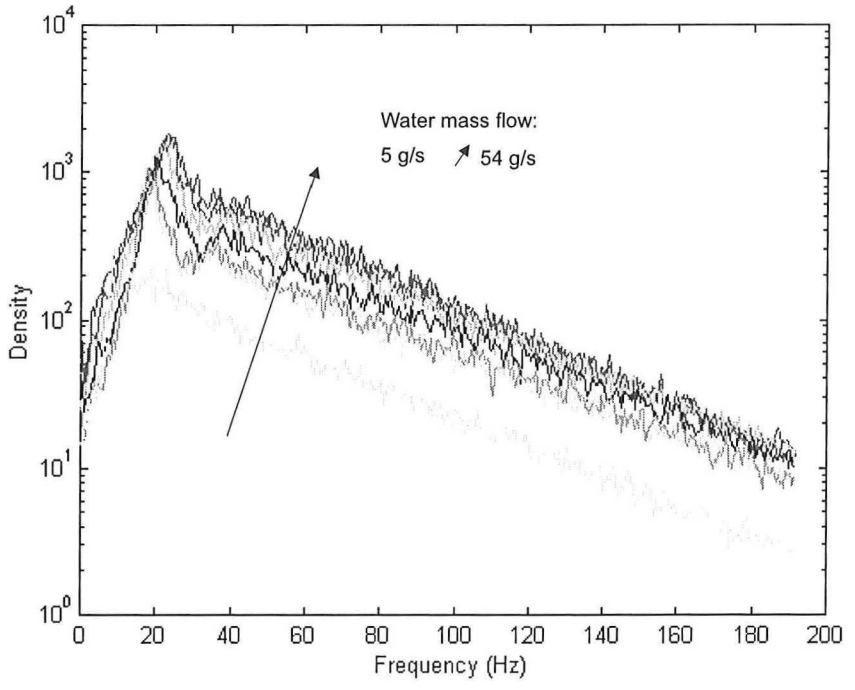

(a) Power spectrum as a function of the water mass flow. Air velocity of 32 m/s. No obstacle inserted.

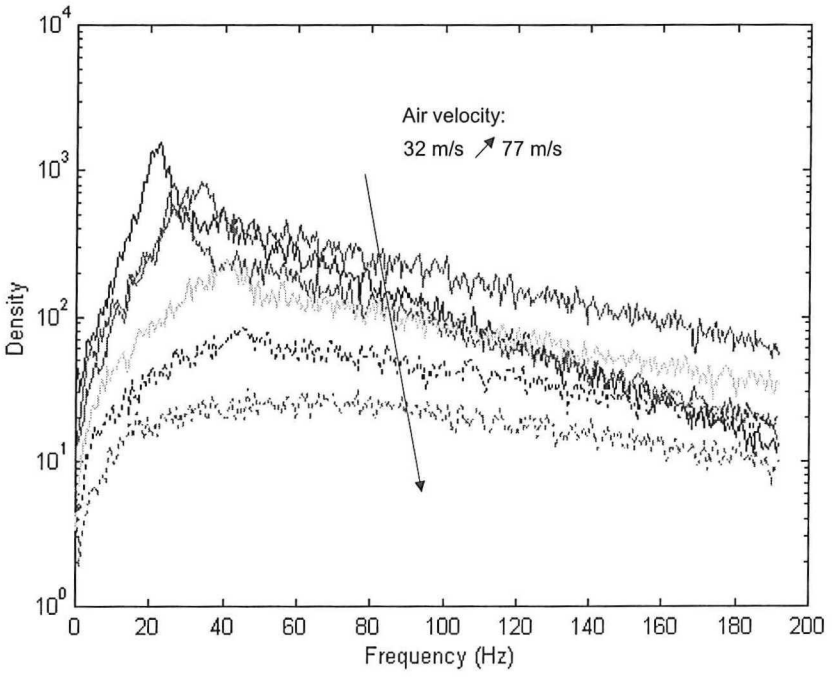

(b) Power spectrum as a function of the air velocity. Water mass flow of 36 g/s. No obstacle inserted.

Figure 4.17: Power spectrum for different water mass flows and different air velocities. No obstacle inserted.

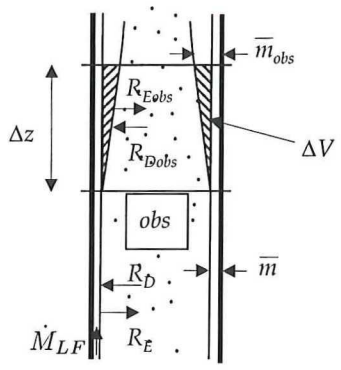

Figure 4.18: Schematic representation for mass balance.

droplet deposition rates $R_{D,obs}/R_D$:

$$\frac{R_{D,obs}}{R_D} = 1 + \frac{\dot{M}_{LF}}{\pi D(D-\overline{m})\Delta z}\frac{1}{R_D}\frac{1}{\overline{m}}\left(\frac{\overline{m}^2}{6} - \frac{\overline{m}_{obs}^2}{12} - \frac{\overline{m}\cdot\overline{m}_{obs}}{12} + \frac{D}{4}(\overline{m}_{obs} - \overline{m})\right) \tag{4.18}$$

In literature [Schadel et al., 1990], an empirical expression is found for the deposition rates in a vertical annular flow:

$$R_D = \frac{0.034}{D^{0.6}}\frac{\dot{M}_E}{u_G \pi D^2/4} \qquad for \qquad \frac{\dot{M}_E}{u_G \pi D^2/4} \leq \frac{0.078}{D^{0.6}} \tag{4.19}$$

$$R_D = \frac{0.021}{D^{0.6}} \qquad for \qquad \frac{\dot{M}_E}{u_G \pi D^2/4} > \frac{0.078}{D^{0.6}} \tag{4.20}$$

The increase in the droplet deposition rates is presented in figure 4.19 as a function of the water mass flow. Instead of the measured entrained mass flow, which is overestimated, a corrected one is used in the preceding equations: the measured entrained mass flow at 4.7 g/s is subtracted from the measured values in order to have zero entrainment close and below the critical mass flow. The effect of the correction on $R_{D,obs}/R_D$ is less than 10%.
The increase in the droplet deposition rates increases with the water mass flow, which is expected, as the concentration in droplets increases with water mass flow. The increase in the deposition rates is larger at 16 cm than at 6 cm above the obstacle; the increase in the droplet deposition is not sensed directly above the obstacle (see the increase in mean film thickness in section 4.4.1). This is not the case for an air velocity of 32 m/s and this is contrary to expectations. The shape of the curve, however, is correct: the increase of the mean film thickness is less sensible for large water mass flows due to the higher droplet concentration (a decreasing ability to follow the gas-phase turbulence for larger droplets by coalescence and a dampening of the gas-phase turbulence by droplet-droplet interaction, see section 4.4.1). This excessively high increase in the droplet deposition rates for an air velocity of 32 m/s may be caused by a false assumption of a linear film height increase between 0, 6 and 16 cm. The increase in the droplet deposition rates is maximum 1.65.

Consider the flow configuration in a Boiling Water Reactor, in which the film on the fuel rods is so thin that disturbance waves do not exist on its surface. The entrainment of liquid from the liquid film is negligible. Evaporation at the film interface is consequently the only source of film depletion. The film dries out if the droplet deposition rate does not balance the evaporation rate. It is assumed in this case that water is at saturation temperature or that heating of the subcooled

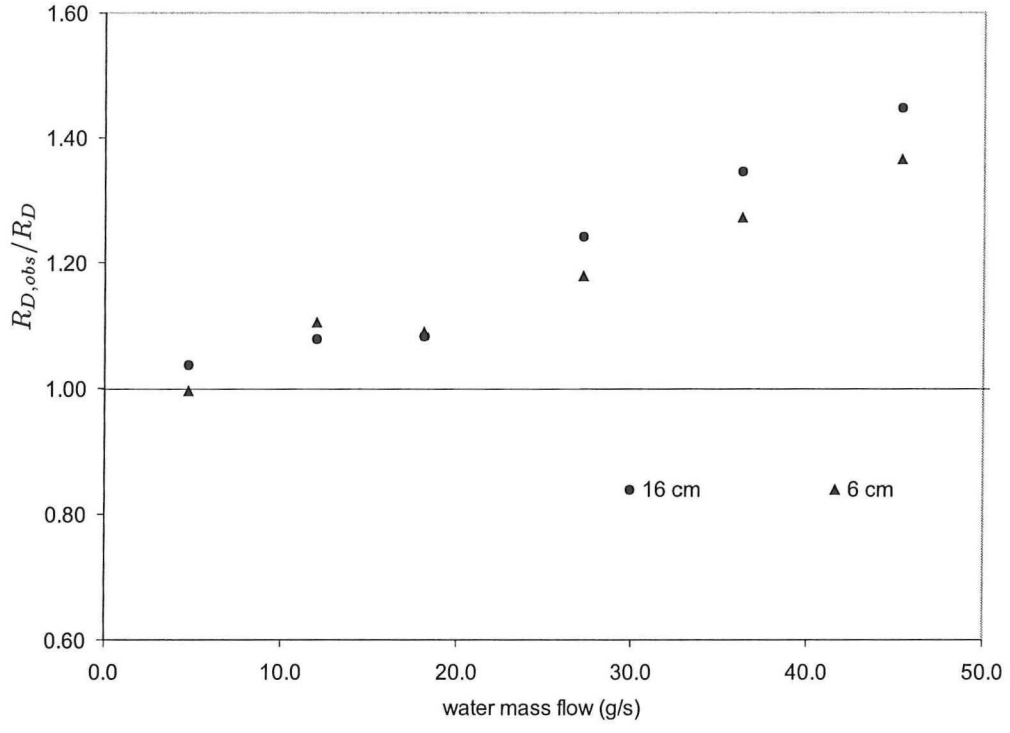

(a) Droplet deposition rate increase as a function of the water mass flow. Air velocity of 61 m/s.

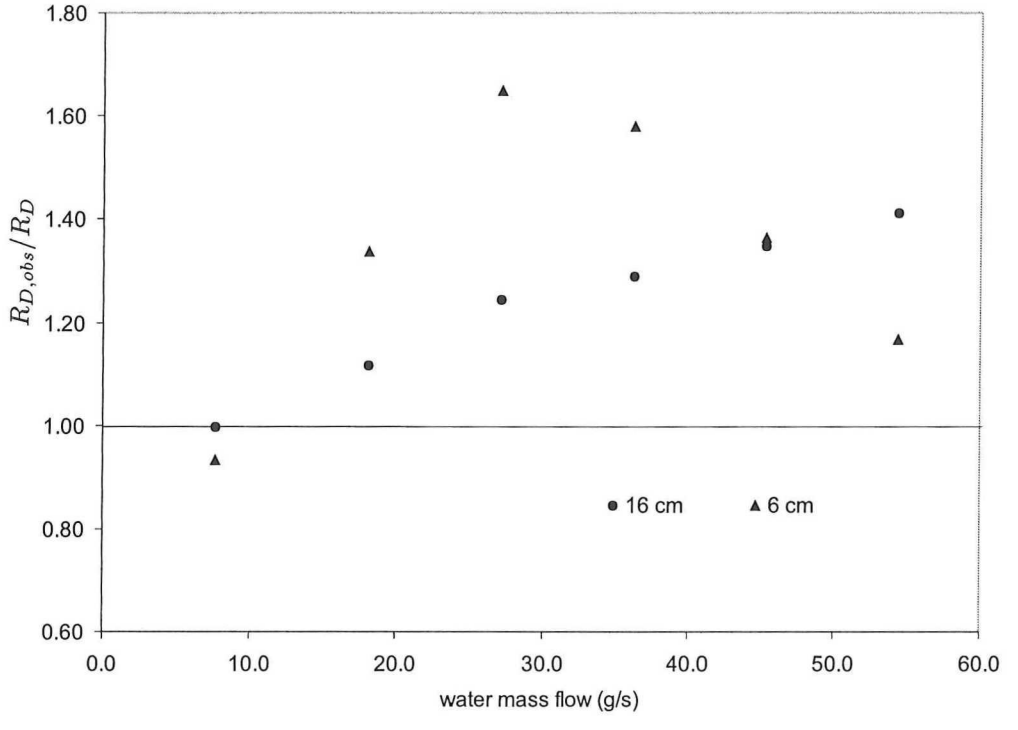

(b) Droplet deposition rate increase as a function of the water mass flow. Air velocity of 32 m/s.

Figure 4.19: Increase in the droplet deposition rates.

liquid in the film is negligible. One can derive from the mass balance (see section 2.5):

$$\frac{d\dot{M}_{LF}}{dz} = (k_D C - R_E - \frac{q''}{H_{LG}})\pi D \tag{4.21}$$

When the gradient in the mass flow and the entrainment rate are negligible, one finds:

$$\frac{q''}{H_{LG}} = k_D C \qquad or \qquad \frac{q''_{obs}}{q''} = \frac{R_{D,obs}}{R_D} \tag{4.22}$$

One can postulate that the relative CHF enhancement equals the relative increase in the deposition rates, which is smaller than 65%, according to figure 4.19. However, in literature [Guo et al., 2001], an enhancement of 250 to 350% is stated when obstacles are used in the zone of the dryout type of crisis. In addition, the obstacle shapes in [Guo et al., 2001] may be less performing than the one used in this study, as they strip more liquid off the wall and block less droplets in the core center compared to the cylinder obstacle used in this research.

However, a BWRs works at much higher liquid temperature and pressure than in this research, which results in an increase of the droplet concentration. Droplet break-up from the film is favored in BWRs, as (i) higher temperatures decrease both the viscosity and the surface tension and (ii) higher pressures may influence positively the break-up mechanisms. With higher droplet concentrations in the vapor phase of the BWR, more droplets can be deposited and higher CHF enhancements can be attained.
Furthermore, other phenomena can lead to CHF enhancement, as:

- turbulence increases the convective heat transfer to the vapor phase and so reduces the heat left for evaporation.
- saturation of the unsaturated fresh water in the film coming from the deposited droplets.

The prediction of the CHF enhancement differs significantly from experimental results of [Guo et al., 2001], probably due to the differences in the droplet concentration. Instead of comparing the droplet deposition rate, one can compare the increase by the obstacle in the droplet deposition constant, k_D, found in this research with predicted ones from literature. k_D is independent of the droplet concentration, C, in the expression of the droplet deposition rate, R_D. In literature [Guo et al., 2001], the droplet deposition constant with obstacle, $k_{D,obs}$, is calculated from the relationship of Windecker et al. (1999):

$$\frac{k_{D,obs}}{k_D} = 1 + 1.4416 \cdot \epsilon \tag{4.23}$$

where ϵ is the blockage ratio, equal to 25% in this research and 12% in [Guo et al., 2001]. Note that the validity of this expression is questionable as the film mass flow and the gas velocities are not included in the correlation.
One needs the droplets concentration, C, to determine the droplet deposition constant from the droplet deposition rate. This one, expressed as mass per unit volume, is derived from the entrained mass flow, $\dot{M}_E$, by the relationship:

$$C = \frac{\dot{M}_E}{s \cdot u_G \pi D^2/4} \tag{4.24}$$

where s is the ratio of the drop velocity to the gas velocity.
In appendix B, it is demonstrated that the difference in the droplet concentration downstream

the obstacle compared to upstream the obstacle is negligible in the experiments of this research. Consequently, the increase in the droplet deposition constant equals the increase in the droplet deposition rate:

$$\frac{k_{D,obs}}{k_D} \approx \frac{R_{D,obs}}{R_D} \tag{4.25}$$

One finds the same order of magnitude in this research and in literature, which gives a value of 1.36 with the relationship of Windecker et al.(1999). In addition to the correlation of Windecker et al. (1999), it is noted that the gas velocity and the droplet concentration (through the water mass flow) influence the increase in the droplet deposition constant.

Chapter 5

Conclusions and recommendations

5.1 Conclusions

In a boiler, the presence of an obstacle in its coolant flow postpones the emergence of liquid film dryout. The delay is probably due to increased rates of droplet deposition. In this research, the effects of an obstacle on the droplet deposition on a vertical water-air annular tube flow in equilibrium are studied. Specifically, the research attempts:

- to verify and quantify the increase in film thickness by droplet deposition.
- to set up an appropriate flow-loop and to investigate the applicability of some measurements techniques.

From the measurements, it can be concluded for the obstacle effects on the annular flow in equilibrium:

1. Inserting the obstacle affects positively the film thickness.
   - The mean film thickness is increased by 15% for low air velocities (32 to 40 m/s) and by about 25% for higher air velocities (61 to 77 m/s).
   - The maximum height of the disturbance waves is rather not affected by forced droplet deposition; whereas the substrate film, that is, the film layer on which the waves are traveling, is.
2. Inserting the obstacle does not affect the interfacial structure.
   - The velocity of the disturbance waves is not changed by the obstacle.
   - The film shape, more particularly the separation between successive disturbance waves, is not changed by the obstacle.
3. One must treat the results with caution. The precision of the measurement techniques, for instance the conductance probes, is not significantly lower than the film increase when inserting the obstacle.

4. The increase in the droplet deposition constant, k_D, in the measurements varies between 1 and 1.65, depending on the water mass flow and the gas velocity, which agrees reasonably well with the one calculated from the Windecker et al. (1999) correlation equal to 1.36. In supplement of that model, it is showed that the increase in the droplet deposition constant and the extent depend on (i) the gas velocity and (ii) the droplet concentration before the obstacle.

5. Using the results of this research, the predicted CHF enhancement appears to be much smaller than the one in literature. However, one must know that the temperature and pressure in a BWR are much higher than in this research. A higher temperature and pressure influence positively the entrainment rates (by a smaller water surface tension, water viscosity and by the break-up mechanisms), hence the droplet concentration and the droplet deposition rates. Therefore, it is proposed (i) to add surfactants in order to simulate BWR conditions, as surfactants will reduce the surface tension and hence increase the droplet concentration in the core and (ii) to continue the measurements with tap water in order to validate the measurements with literature.

5.2 Recommendations

The film thickness appears to be increased by the obstacle. However, more detailed measurements are necessary to obtain accurately the hydrodynamics induced by the obstacle on the annular flow. The flow-loop in this research is well suited for studying intensively droplet deposition, although this should take into account the following recommendations:

1. Improvement of the flow-loop.
   - Use of longer segments to reduce as far as possible the perturbations introduced by segments transitions.
   - Use of a film withdrawal device with more and larger outlets. A vacuum pump could help to the film removal, but in that case one must take care of the pressure effects [Yano et al.,].
   - Use of a pressurized air-water separator in order to maintain the pressure at the outlet (consequently in the tube) constant. This ensures that errors in the measurements due to atmospheric pressure changes are avoided.
   - Use of obstacles of different shape and of different blockage ratio in order to optimize forced droplet deposition by the obstacle.

2. Improvement of the conductance probes technique.
   - Use of radial conductance probes, in which the receiver is made of a segmented ring, this in order to take into account asymmetrical behavior of the waves and to avoid the corresponding errors due to circumferential averaging.
   - Installation of a calibration probe on-line to correct changes in water conductivity (due to temperature changes and to gas dissolution). For this, injected water or removed film water must pass through an annulus, on which the same type of electrodes are mounted and of which the gap length is known.
   - Second possibility relative to water conductivity is to inject salt and to maintain its concentration constant in the flow-loop. Drawback is that physical properties are changed, as for instance the surface tension, which can be of importance for the wave structure.

- Performance of detailed calibrations and repetition of measurements to inform on the measurements errors by the conductance probes. Research of other possible errors (for instance, of electrical components in the conductance probes hardware).

3. Use of Laser-Doppler Anemometry (LDA) to inform on:

   - The velocity profile in the liquid film.
   - The increase in turbulence in the gas flow due to the obstacle, this to allow rough predictions of the increase in the convective heat transfer to the vapor phase.
   - Combination of LDA with the conductance probes technique in order to analyze the LDA results.

4. Determination of the axial variation in the liquid film mass flow by using the film withdrawal device at different distances relative to the obstacle.

5. Use of techniques to study the droplets behavior in equilibrium flow and in obstacle-disturbed flow, for instance by Phase-Doppler Anemometry (PDA) [Fore and Dukler, 1995b]. This is desirable to understand the droplet deposition mechanism, as their size and interaction may influence the deposition.

Appendix A

CHF correlations

A.1 The Bowring correlation

Bowring (1972):

$$q''_{CHF} = \frac{A - DGH_{LG}x/4}{C} \tag{A.1}$$

with;

$$A = 2.317\left(\frac{DGH_{LG}}{4}\right)\frac{F_1}{1+0.0143F_2D^{1/2}G} \tag{A.2}$$

$$C = \frac{0.077F_3DG}{1+0.347F_4\left(\frac{G}{1356}\right)^{2-0.00725p}} \tag{A.3}$$

where F_1, F_2, F_3 and F_4 are tabulated as a function of p.
Valid for the following range of variables:

$p\ (bar)$	$2-190$
$D\ (m)$	$0.002-0.045$
$L\ (m)$	$0.15-3.7$
$G\ (kg{\cdot}m^{-2}{\cdot}s^{-1})$	$136-18600$

A.2 The Biasi correlation

Biasi et al. (1967):
for low qualities:

$$q''_{CHF} = \frac{1.883{\cdot}10^7}{D^nG^{1/6}}\left(\frac{f(p)}{G^{1/6}} - x(z)\right) \tag{A.4}$$

for high qualities:

$$q''_{CHF} = \frac{3.78{\cdot}10^7h(p)}{D^nG^{0.6}}\left(1 - x(z)\right) \tag{A.5}$$

using the parameters:

$n = 0.4$	$D \geq 1cm$
$n = 0.6$	$D < 1cm$
$f(p)$	$0.7249 + 0.099pexp(-0.032p)$
$h(p)$	$-1.159 + 0.149pexp(-0.019p) + 8.99p/(10 + p^2)$

Valid for the following range of variables:

$p\ (bar)$	$2.7 - 140$
$D\ (m)$	$0.003 - 0.0375$
$L\ (m)$	$0.2 - 6$
$G\ (kg{\cdot}m^{-2}{\cdot}s^{-1})$	$100 - 6000$
x_{cr}	$1/(1 + \rho_L/\rho_G) < x_{cr} < 1$

A.3 The Katto correlation

Katto and Ohno (1984):

$$q''_{CHF} = XG(H_{LG} + K(\Delta H_{SUB})_i) \tag{A.6}$$

where the terms X and K are functions of three dimensionless groupings:

$$Z' = L/D \tag{A.7}$$

$$R' = \rho_G/\rho_L \tag{A.8}$$

$$W' = \frac{\sigma\rho_L}{G^2 L} \tag{A.9}$$

The value of X equals one of five possible values of X, the value of K one of three values of K, the choice depending on the conditions.

$$X_1 = \frac{CW'^{0.043}}{Z'} \tag{A.10}$$

$$X_2 = \frac{0.1R'^{0.133}W'^{0.333}}{1 + 0.0031Z'} \tag{A.11}$$

$$X_3 = \frac{0.098R'^{0.133}W'^{0.433}Z'0.27}{1 + 0.0031Z'} \tag{A.12}$$

$$X_4 = \frac{0.00384R'^{0.6}W'^{0.173}}{1 + 0.28W'^{0.233}Z'} \tag{A.13}$$

$$X_5 = \frac{0.234R'^{0.513}W'^{0.433}Z'^{0.27}}{1 + 0.0031Z'} \tag{A.14}$$

$$K_1 = \frac{0.261}{CW'^{0.043}} \tag{A.15}$$

$$K_2 = \frac{0.833(0.0124 + 1/Z')}{R'^{0.133} W'^{0.333}} \tag{A.16}$$

$$K_3 = \frac{1.12(1.52 W'^{0.233} + 1/Z')}{R'^{0.6} W'^{0.173}} \tag{A.17}$$

where

$$\begin{array}{cc} C = 0.25 & \text{for } Z' < 50 \\ C = 0.25 + 0.0009(Z' - 50) & \text{for } 50 < Z' < 150 \\ C = 0.34 & \text{for } Z' > 150 \end{array}$$

$R' < 0.15$		$R' > 0.15$	
$X_1 < X_2$	$X = X_1$	$X_1 < X_5$	$X = X_1$
$X_1 > X_2$ and $X_2 < X_3$	$X = X_2$	$X_1 > X_5$ and $X_5 > X_4$	$X = X_5$
$X_1 > X_2$ and $X_2 > X_3$	$X = X_3$	$X_1 > X_5$ and $X_5 < X_4$	$X = X_4$
$K_1 > K_2$	$K = K_1$	$K_1 > K_2$	$K = K_1$
$K_1 < K_2$	$K = K_2$	$K_1 < K_2$ and $K_2 < K_3$	$K = K_2$
		$K_1 < K_2$ and $K_2 > K_3$	$K = K_3$

Valid for the following range of variables:

$$\begin{array}{c} 0.01 < L < 8.8\ (m) \\ 0.001 < D < 0.038\ (m) \\ 5 < Z' < 880 \\ 0.0003 < R' < 0.41 \\ 3{\cdot}10^{-9} < W' < 2{\cdot}10^{-2} \end{array}$$

Appendix B

Supplement to section 4.7: Droplet concentration downstream the obstacle

When the obstacle is inserted, a linear decrease in the concentration is assumed between the obstacle and the measurement points. Then, the concentration C_{obs} is assumed equal to:

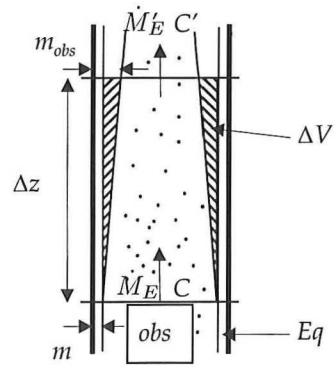

Figure B.1: Schematic representation for mass balance.

$$C_{obs} = \frac{C + C'}{2} \tag{B.1}$$

where C and C' are respectively the concentrations at the obstacle and at the measurement point. Consequently:

$$\frac{C_{obs}}{C} = \frac{1}{2}\left(1 + \frac{\dot{M}'_E}{\dot{M}_E}\right) \tag{B.2}$$

where $\dot{M}_E$ and $\dot{M}'_E$ are respectively the entrained mass flows at the obstacle location and at one of the measurement points. One obtains from a mass balance between the obstacle and the measurement point (see figure B.1):

$$\dot{M}_E - \dot{M'}_E = \rho_L \overline{u} \frac{\Delta V}{\Delta z} \tag{B.3}$$

which can be written as:

$$\frac{\dot{M'}_E}{\dot{M}_E} = 1 - \frac{\dot{M}_{LF}}{\dot{M}_E} \frac{1}{D\overline{m}} \left[\frac{\overline{m}^2}{6} - \frac{\overline{m}_{obs}^2}{12} - \frac{\overline{m} \cdot \overline{m}_{obs}}{12} + \frac{D}{4} (\overline{m}_{obs} - \overline{m}) \right] \tag{B.4}$$

The results show that the ratio $\dot{M'}_E / \dot{M}_E$ is very close to 1. The difference in the droplet concentration downstream the obstacle compared to the one in equilibrium upstream the obstacle is negligible.

Bibliography

Andreani, M., and Yadigaroglu, G., 1994, Prediction methods for dispersed flow film boiling: *Int. J. Multiphase Flow*, **20, Suppl.**, 1–51.

Asali, J. C., Hanratty, T. J., and Andreussi, P., 1985, Interfacial drag and film height for vertical annular flow: *AIChE J.*, **31(6)**, 895–902.

Azzopardi, B. J., 1986, Disturbance wave frequencies, velocities and spacing in vertical annular two-phase flow: *Nucl. Eng. Des.*, **92**, 121–133.

Binder, J. L., and Hanratty, T. J., 1991, A diffusion model for droplet deposition in gas/liquid annular flow: *Int. J. Multiphase Flow*, **17, 1**, 1–11.

Brown, R. C., Andreussi, P., and Zanelli, S., 1978, The use of wire probes for the measurement of liquid film thickness in annular gas-liquid flows: *Can. J. Chem. Eng.*, **130(9)**, 754–757.

Celata, G. P., Cumo, M., Mariani, A., and Zummo, G., 2000, Burnout in subcooled flow boiling of water. A visual experimental study: *Int. J. Therm. Sci.*, **39**, 896–908.

Collier, J. G., and Thome, J. R., 1994, *Convective boiling and condensation, Ch. 8 and 9*: Clarendon, Oxford.

Coney, M. W. E., 1973, The theory and application of conductance probes for the measurement of liquid film thickness in two-phase flow: *J. Physics, E: Sci. Instrum.*, **6**, 903–910.

Corradini, M. L., 1997, Burnout and the Critical Heat Flux: *nsrc-webmaster@loca.neep.wisc.edu.*

Deelder, B., 2001, *Measurements on the turbulent flow through and around monoliths for application in a monolith stirred reactor*: MsC. thesis, Delft University of Technology.

Doerffer, S., Groeneveld, D. C., and Schenk, J. R., 1996, Experimental study on the effects on flow inserts on heat transfer and critical heat flux: *Proc. Int. Conf. Nucl. Eng. ASME*, **1, Part A**, 41–49.

Drain, L. E., 1980, *The laser Doppler technique*: Wiley, Chichester.

Fore, L. B., and Dukler, A. E., 1995a, Droplet deposition and momentum transfer in annular flow: *AIChE J.*, **41(9)**, 2040–2047.

——— 1995b, Droplet deposition and momentum transfer in annular flow: *Int. J. Multiphase Flow*, **21(2)**, 137–149.

Groeneveld, D. C., and Snoek, C. W., 1986, *Multiphase science and technology; Chapter : A comprehensive examination of heat transfer correlations suitable for reactor safety analysis*: Hewitt, G. F. et al.

Groeneveld, D. C., Leung, L. K. H., Kirillov, P. L., Bobkov, V. P., Smogalev, I. P., Vinogradov, V. N., Huang, X. C., and Royer, E., 1996, The 1995 look-up table for critical heat flux in tubes: *Nucl. Eng. Des.*, **163**, 1–23.

Groeneveld, D. C., 1992, *Post-dryout heat transfer; Chapter : A review in inverted annular and low quality film boiling*: Hewitt, Delhaye, Zuber.

Guo, Y., Groeneveld, D. C., and Cheng, S. C., 2001, Prediction of CHF enhancement due to flow obstacles: *Internal report.*

IAEA, 2001, Thermohydraulic relationships for advanced water cooled reactors: *IAEA-TECDOC-1203*, pages 1–108.

Katto, Y., 1994, Critical Heat Flux: *Int. J. Multiphase Flow*, **20, Suppl.**, 53–90.

Kockx, J., 1999, *Experiments on the gas exchange between a Taylor bubble and its liquid slug in a vertical tube*: PhD. thesis, Delft University of Technology.

Pioro, J. L., Cheng, S. C., Vasic, A. Z., and Salah, I., 1999, Experimental evaluation of the limiting critical quality in circular and non-circular flow geometries: *Nucl. Eng. Des.*, **190**, 317–339.

Pioro, J. L., Groeneveld, D. C., Cheng, S. C., Doerffer, S., and Vasic, A. Z., 2000, Effect of flow obstruction shape on the critical heat flux: *Proc. Int. Conf. Nucl. Eng. ICONE 8*, **6, Part A**, 135–149.

Prasser, H. M., Boettger, A., and Zschau, J., 1998, A new electrode-mesh tomograph for gas-liquid flows: *Flow Meas. and Instrum.*, **9**, 111–119.

Raffel, M., Willert, C., and Kompenhans, J., 1998, *Particle image velocimetry*: Ed. Springer.

Schadel, S. A., Leman, G. W., Binder, J. L., and Hanratty, T. J., 1990, Rates of atomization and deposition in vertical annular flow: *Int. J. Multiphase Flow*, **16(3)**, 363–374.

Shedd, T. A., and Newell, T. A., 1998, Automated optical liquid film thickness measurement method: *Rev. Sci. Instrum.*, **69(12)**, 4205–4213.

Wolf, A., Jayanti, S., and Hewitt, G. F., 1996, On the nature of ephemeral waves in vertical annular flow: *Int. J. Multiphase Flow*, **22(2)**, 325–333.

Yano, T., Aritomi, M., Kikura, H., and Obata, H., Mechanistic modeling for ring-type boiling water reactor fuel spacer design (3) run-off effect and model formulation: *Nucl. Eng. Des.*, **210**, 21–36.